3D Scanning for Personal 3D Printing: Build Your Own Desktop 3D Scanner

Gabriel Taubin
Brown University
taubin@brown.edu

Daniel Moreno
Brown University
daniel_moreno@brown.edu

Douglas Lanman
Oculus VR R&D
http://dlanman.info

Version 1.0 June 11 2014
Download latest version from http://mesh.brown.edu/desktop3dscan

Siggraph 2014 Studio Course

Abstract

3D Printing has entered the mainstream. Multiple low cost desktop 3D printers are currently available from various vendors, and open source projects let hobbyists build their own. This course addresses the problem of creating 3D models for 3D printing. As is the case for 3D printers, low-cost homemade 3D scanners are now within reach of students and hobbyists with a modest budget. This course provides the students with the necessary mathematics, software, and practical details to leverage projector-camera systems to build their own desktop 3D scanner. An example-driven approach is used throughout, with each new concept illustrated using a practical scanner implemented with off-the-shelf parts. First, the mathematics of triangulation is explained using the intersection of parametric and implicit representations of lines and planes in 3D. The particular case of ray-plane triangulation is illustrated using a scanner built with a single camera and a modified laser pointer. Camera calibration is explained at this stage to convert image measurements to geometric quantities. The mathematics of rigid-body transformations are covered through this example. Next, the details of projector calibration are explained through the development of a classic structured light scanning system using a single camera and projector pair. A minimal post-processing pipeline is described to convert the point-based representations produced by these scanners to watertight meshes. Key topics covered in this section include: surface representations, file formats, data structures, polygonal meshes, and basic smoothing and gap-filling operations. The course concludes with the description of some commercially available low cost desktop 3D scanners.

Prerequisites

Attendees should have a basic undergraduate-level understanding of linear algebra. While executables are provided for beginners, attendees with prior knowledge of Matlab, C/C++, and Java programming will be able to directly examine and modify the provided source code.

Course Speakers

Gabriel Taubin
Brown University, taubin@brown.edu, http://mesh.brown.edu/taubin

Gabriel Taubin is Associate Professor of Engineering and Computer Science at Brown University. He earned a Licenciado en Ciencias Matemticas degree from the University of Buenos Aires, Argentina, and a Ph.D. degree in Electrical Engineering from Brown University. He was named IEEE Fellow for his contributions to three-dimensional geometry compression technology and multimedia standards, won the Eurographics 2002 Günter Enderle Best Paper Award, and was named IBM Master Inventor. From January 2010 to December 2013 he served as Editor-in-Chief of the IEEE Computer Graphics and Applications Magazine. He also serves as member of the Editorial Board of the Geometric Models journal, and has served as associate editor of the IEEE Transactions of Visualization and Computer Graphics. From 1990 to 2003 he held various positions at the IBM T.J. Watson Research Center, including Research Staff Member and Research Manager. He was appointed Visiting Professor of Electrical Engineering at Caltech during the 2000-2001 academic year, Visiting Associate Professor of Media Arts and Sciences at the MIT Media Lab during the Spring semester of 2010, Visiting Professor of Computer Science at the University of Buenos Aires, during the Spring semester of 2013. In 2014 he won a Fulbright Specialist grant. He has authored numerous reviewed book chapters, journal, or conference papers, and is a co-inventor of 48 international patents. He has made significant theoretical and practical contributions to the field now called Digital Geometry Processing, comprising: 3D shape capturing and surface reconstruction, geometric modeling, geometry compression, progressive transmission, signal processing, and display of discrete surfaces. He teaches courses on 3D Photography and Digital Geometry Processing at Brown University on a regular basis.

Daniel Moreno
Brown University, daniel_moreno@brown.edu

Daniel A. Moreno received a degree of Licenciado en Ciencias de la Computacion from Universidad Nacional de Rosario, Argentina, in 2011. The same year, he joined Brown University where he is currently pursuing a PhD in Engineering. His research topic is Computer Vision, specifically the area of 3D models acquisition and processing. Recently, he has been working on structured-light systems calibration and low-cost 3D scanners. He has written a fully functional opensource 3D scanning software and collaborated with the implementation of the Smooth Signed Distance surface reconstruction algorithm. His work experience includes internships at Evolution Robotics in 2008, and NVIDIA Corp. in the summer of 2013.

Contributing to Lecture Notes

Douglas Lanman
Research Scientist, Oculus VR R&D, http://dlanman.info

Douglas Lanman is a Research Scientist at Oculus VR R&D. His research is focused on computational displays and imaging systems, emphasizing compact optics for head-mounted displays (HMDs), glasses-free 3D displays, light field cameras, and active illumination for 3D reconstruction and interaction. He received a B.S. in Applied Physics with Honors from Caltech in 2002 and M.S. and Ph.D. degrees in Electrical Engineering from Brown University in 2006 and 2010, respectively. He was a Senior Research Scientist at NVIDIA from 2012 to 2014, a Postdoctoral Associate at the MIT Media Lab from 2010 to 2012, and an Assistant Research Staff Member at MIT Lincoln Laboratory from 2002 to 2005. He has worked as an intern at Intel, Los Alamos National Laboratory, INRIA Rhne-Alpes, Mitsubishi Electric Research Laboratories (MERL), and the MIT Media Lab. Douglas has presented the following SIGGRAPH courses: "Build Your Own 3D Scanner" (2009), "Build Your Own 3D Display" (2010, 2011), "Computational Imaging" (2012), "Computational Displays" (2012), and "Put on Your 3D Glasses Now: The Past, Present, and Future of Virtual and Augmented Reality" (2014).

Contents

1 Introduction **1**
- 1.1 3D Scanning Technology . . . 1
  - 1.1.1 Passive Methods . . . 2
  - 1.1.2 Active Methods . . . 3
- 1.2 3D Scanners studied in this Course . . . 5

2 The Mathematics of Triangulation **7**
- 2.1 Perspective Projection and the Pinhole Model . . . 7
- 2.2 Geometric Representations . . . 7
  - 2.2.1 Points and Vectors . . . 8
  - 2.2.2 Parametric Representation of Lines and Rays . . . 8
  - 2.2.3 Parametric Representation of Planes . . . 9
  - 2.2.4 Implicit Representation of Planes . . . 10
  - 2.2.5 Implicit Representation of Lines . . . 10
- 2.3 Reconstruction by Triangulation . . . 10
  - 2.3.1 Line-Plane Intersection . . . 11
  - 2.3.2 Line-Line Intersection . . . 12
- 2.4 Coordinate Systems . . . 14
  - 2.4.1 Image Coordinates and the Pinhole Camera . . . 14
  - 2.4.2 The Ideal Pinhole Camera . . . 15
  - 2.4.3 The General Pinhole Camera . . . 15
  - 2.4.4 Lines from Image Points . . . 17
  - 2.4.5 Planes from Image Lines . . . 17

3 Camera and Projector Calibration **19**
- 3.1 Camera Calibration . . . 19
  - 3.1.1 Camera selection and interfaces . . . 19
  - 3.1.2 Calibration Methods and Software . . . 21
  - 3.1.3 Calibration Procedure . . . 22
- 3.2 Projector Calibration . . . 24
  - 3.2.1 Projector Selection and Interfaces . . . 24
  - 3.2.2 Calibration Software and Procedure . . . 25

4 The Laser Slit 3D Scanner **28**
- 4.1 Description . . . 28
- 4.2 Turntable calibration . . . 29
  - 4.2.1 Camera extrinsics . . . 31
  - 4.2.2 Center of rotation and rotation angle . . . 32

4.2.3 Global optimization . . . 33
4.3 Image Laser Detection . . . 33
4.4 Background detection . . . 35
4.5 Plane of light calibration . . . 36
4.6 3D model reconstruction . . . 37

5 Structured Lighting **39**
5.1 Structured Light Scanner . . . 39
5.1.1 Scanner Hardware . . . 39
5.1.2 Structured Light Sequences . . . 40
5.2 Image Processing . . . 42
5.3 Calibration . . . 44
5.4 Reconstruction . . . 44
5.5 Sample software . . . 45

6 Surfaces from Point Clouds **47**
6.1 Representation and Visualization of Point Clouds . . . 47
6.1.1 File Formats . . . 47
6.1.2 Visualization . . . 48
6.2 Merging Point Clouds . . . 48
6.2.1 Computing Rigid Body Matching Transformations . . . 49
6.2.2 The Iterative Closest Point (ICP) Algorithm . . . 50
6.3 Surface Reconstruction from Point Clouds . . . 51
6.3.1 Continuous Surfaces . . . 51
6.3.2 Discrete Surfaces . . . 51
6.3.3 Isosurfaces . . . 52
6.3.4 Isosurface Construction Algorithms . . . 52
6.3.5 Algorithms to Fit Implicit Surfaces to Point Clouds . . . 55

7 Conclusion **56**

Bibliography **57**

Chapter 1

Introduction

3D Printing has become a popular subject these days. More and more low cost desktop 3D printers are introduced, and open source projects let hobbyists build their own. Without models, a 3D printer is not really useful. Professionals have access to complete CAD software or modelers that costs thousands and need extensive training. They can also acquire a scene/object using 3D scanners. This course addresses the problem of creating 3D models for 3D printing by copying and modifying existing objects. As is the case for desktop 3D printers this course teaches the mathematical foundations of the various methods used to build 3D scanners, and includes specific instructions to build several low-cost homemade 3D scanners which can produce models of equal or better quality as many commercial products currently in the market.

These course notes are organized into three primary sections, spanning theoretical concepts, practical construction details, and algorithms for constructing high-quality 3D models. Chapters 1 and 2 survey the field and present the unifying concept of triangulation. Chapters 3–5 document the construction of projector-camera systems, slit-based 3D scanners, and 3D scanners based on structured lighting. The post-processing processes for generating polygon meshes from point clouds are covered in Chapter 6.

Revised course notes, updated software, recent publications, and similar do-it-yourself projects are maintained on the course website at http://mesh.brown.edu/desktop3dscan.

1.1 3D Scanning Technology

Metrology is an ancient and diverse field, bridging the gap between mathematics and engineering. Efforts at measurement standardization were first undertaken by the Indus Valley Civilization as early as 2600–1900 BCE. Even with only crude units, such as the length of human appendages, the development of geometry revolutionized the ability to measure distance accurately. Around 240 BCE, Eratosthenes estimated the circumference of the Earth from knowledge of the elevation angle of the Sun during the summer solstice in Alexandria and Syene. Mathematics and standardization efforts continued to mature through the Renaissance (1300–1600 CE) and into the Scientific Revolution (1550–1700 CE). However, it was the Industrial Revolution (1750–1850 CE) which drove metrology to the forefront. As automatized methods of mass production became commonplace, advanced measurement technologies ensured interchangeable parts were just that–accurate copies of the original.

Through these historical developments, measurement tools varied with mathematical knowledge and practical needs. Early methods required direct contact with a surface (e.g., callipers and rulers). The pantograph, invented in 1603 by Christoph Scheiner, uses a special mechani-

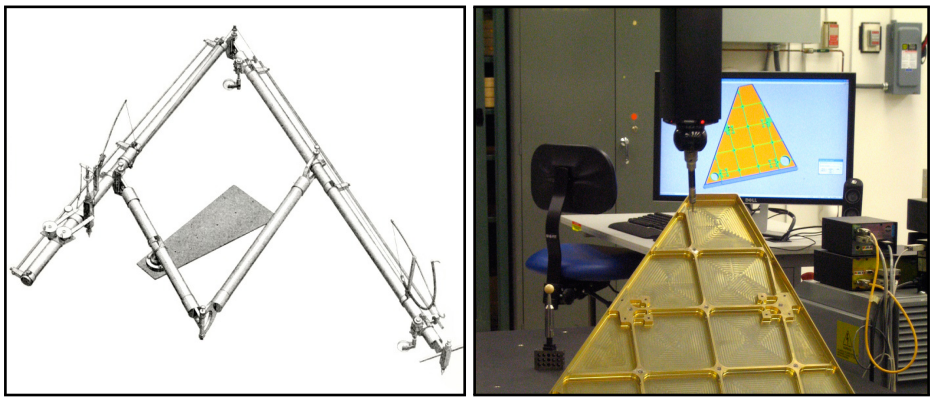

Figure 1.1: Contact-based shape measurement. (Left) A sketch of Sorenson's engraving pantograph patented in 1867. (Right) A modern coordinate measuring machining (from Flickr user hyperbolation). In both devices, deflection of a probe tip is used to estimate object shape, either for transferring engravings or for recovering 3D models, respectively.

cal linkage so movement of a stylus (in contact with the surface) can be precisely duplicated by a drawing pen. The modern coordinate measuring machine (CMM) functions in much the same manner, recording the displacement of a probe tip as it slides across a solid surface (see Figure 1.1). While effective, such contact-based methods can harm fragile objects and require long periods of time to build an accurate 3D model. Non-contact scanners address these limitations by observing, and possibly controlling, the interaction of light with the object.

1.1.1 Passive Methods

Non-contact optical scanners can be categorized by the degree to which controlled illumination is required. Passive scanners do not require direct control of any illumination source, instead relying entirely on ambient light. Stereoscopic imaging is one of the most widely used passive 3D imaging systems, both in biology and engineering. Mirroring the human visual system, stereoscopy estimates the position of a 3D scene point by triangulation [LN04]; first, the 2D projection of a given point is identified in each camera. Using known calibration objects, the imaging properties of each camera are estimated, ultimately allowing a single 3D line to be drawn from each camera's center of projection through the 3D point. The intersection of these two lines is then used to recover the depth of the point.

Trinocular [VF92] and multi-view stereo [HZ04] systems have been introduced to improve the accuracy and reliability of conventional stereoscopic systems. However, all such passive triangulation methods require *correspondences* to be found among the various viewpoints. Even for stereo vision, the development of matching algorithms remains an open and challenging problem in the field [SCD*06]. Today, real-time stereoscopic and multi-view systems are emerging, however certain challenges continue to limit their widespread adoption [MPL04]. Foremost, flat or periodic textures prevent robust matching. While machine learning methods and prior knowledge are being advanced to solve such problems, multi-view 3D scanning remains somewhat outside the domain of hobbyists primarily concerned with accurate, reliable 3D measurement.

Many alternative passive methods have been proposed to sidestep the correspondence problem, often times relying on more robust computer vision algorithms. Under controlled conditions, such as a known or constant background, the external boundaries of foreground objects can be

reliably identified. As a result, numerous shape-from-silhouette algorithms have emerged. Laurentini [Lau94] considers the case of a finite number of cameras observing a scene. The visual hull is defined as the union of the generalized viewing cones defined by each camera's center of projection and the detected silhouette boundaries. Recently, free-viewpoint video [CTMS03] systems have applied this algorithm to allow dynamic adjustment of viewpoint [MBR*00, SH03]. Cipolla and Giblin [CG00] consider a differential formulation of the problem, reconstructing depth by observing the visual motion of occluding contours (such as silhouettes) as a camera is perturbed.

Optical imaging systems require a sufficiently large aperture so that enough light is gathered during the available exposure time [Hec01]. Correspondingly, the captured imagery will demonstrate a limited depth of field; only objects close to the plane of focus will appear in sharp contrast, with distant objects blurred together. This effect can be exploited to recover depth, by increasing the aperture diameter to further reduce the depth of field. Nayar and Nakagawa [NN94] estimate shape-from-focus, collecting a focal stack by translating a single element (either the lens, sensor, or object). A focus measure operator [WN98] is then used to identify the plane of best focus, and its corresponding distance from the camera.

Other passive imaging systems further exploit the depth of field by modifying the shape of the aperture. Such modifications are performed so that the point spread function (PSF) becomes invertible and strongly depth-dependent. Levin et al. [LFDF07] and Farid [Far97] use such coded apertures to estimate intensity and depth from defocused images. Greengard et al. [GSP06] modify the aperture to produce a PSF whose rotation is a function of scene depth. In a similar vein, shadow moiré is produced by placing a high-frequency grating between the scene and the camera. The resulting interference patterns exhibit a series of depth-dependent fringes.

While the preceding discussion focused on optical modifications for 3D reconstruction from 2D images, numerous model-based approaches have also emerged. When shape is known *a priori*, then coarse image measurements can be used to infer object translation, rotation, and deformation. Such methods have been applied to human motion tracking [KM00, OSS*00, dAST*08], vehicle recognition [Sul95, FWM98], and human-computer interaction [RWLB01]. Additionally, user-assisted model construction has been demonstrated using manual labeling of geometric primitives [Deb97].

1.1.2 Active Methods

Active optical scanners overcome the correspondence problem using controlled illumination. In comparison to non-contact and passive methods, active illumination is often more sensitive to surface material properties. Strongly reflective or translucent objects often violate assumptions made by active optical scanners, requiring additional measures to acquire such problematic subjects. For a detailed history of active methods, we refer the reader to the survey article by Blais [Bla04]. In this section we discuss some key milestones along the way to the scanners we consider in this course.

Many active systems attempt to solve the correspondence problem by replacing one of the cameras, in a passive stereoscopic system, with a controllable illumination source. During the 1970s, single-point laser scanning emerged. In this scheme, a series of fixed and rotating mirrors are used to raster scan a single laser spot across a surface. A digital camera records the motion of this "flying spot". The 2D projection of the spot defines, with appropriate calibration knowledge, a line connecting the spot and the camera's center of projection. The depth is recovered by intersecting this line with the line passing from the laser source to the spot, given by the known deflection of the mirrors. As a result, such single-point scanners can be seen as the optical equivalent of coordinate measuring machines.

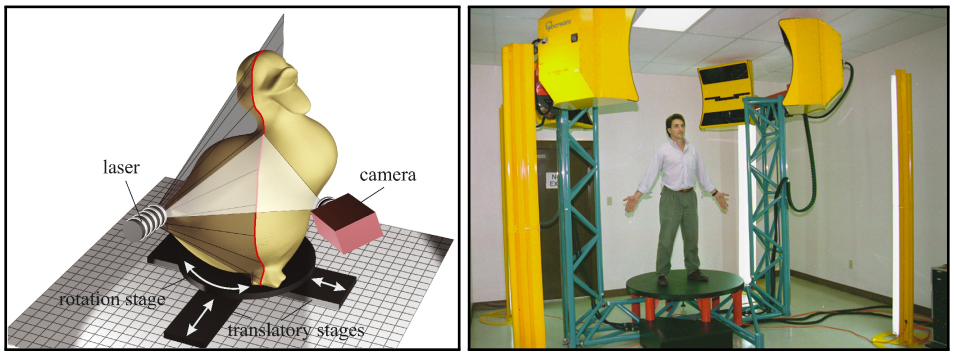

Figure 1.2: Active methods for 3D scanning. (Left) Conceptual diagram of a 3D slit scanner, consisting of a mechanically translated laser stripe. (Right) A Cyberware scanner, applying laser striping for whole body scanning (from Flickr user NIOSH).

As with CMMs, single-point scanning is a painstakingly slow process. With the development of low-cost, high-quality CCD arrays in the 1980s, slit scanners emerged as a powerful alternative. In this design, a laser projector creates a single planar sheet of light. This "slit" is then mechanically-swept across the surface. As before, the known deflection of the laser source defines a 3D plane. The depth is recovered by the intersection of this plane with the set of lines passing through the 3D stripe on the surface and the camera's center of projection.

Effectively removing one dimension of the raster scan, slit scanners remain a popular solution for rapid shape acquisition. A variety of commercial products use swept-plane laser scanning, including the Polhemus FastSCAN [Pol], the NextEngine [Nex], the SLP 3D laser scanning probes from Laser Design [Las], and the HandyScan line of products [Cre]. While effective, slit scanners remain difficult to use if moving objects are present in the scene. In addition, because of the necessary separation between the light source and camera, certain occluded regions cannot be reconstructed. This limitation, while shared by many 3D scanners, requires multiple scans to be merged—further increasing the data acquisition time.

A digital "structured light" projector can be used to eliminate the mechanical motion required to translate the laser stripe across the surface. Naïvely, the projector could be used to display a single column (or row) of white pixels translating against a black background to replicate the performance of a slit scanner. However, a simple swept-plane sequence does not fully exploit the projector, which is typically capable of displaying arbitrary 24-bit color images. Structured lighting sequences have been developed which allow the projector-camera correspondences to be assigned in relatively few frames. In general, the identity of each plane can be encoded spatially (i.e., within a single frame) or temporally (i.e., across multiple frames), or with a combination of both spatial and temporal encodings. There are benefits and drawbacks to each strategy. For instance, purely spatial encodings allow a single static pattern to be used for reconstruction, enabling dynamic scenes to be captured. Alternatively, purely temporal encodings are more likely to benefit from redundancy, reducing reconstruction artifacts. We refer the reader to a comprehensive assessment of such codes by Salvi et al. [SPB04].

Both slit scanners and structured lighting are ill-suited for scanning dynamic scenes. In addition, due to separation of the light source and camera, certain occluded regions will not be recovered. In contrast, time-of-flight rangefinders estimate the distance to a surface from a single center of projection. These devices exploit the finite speed of light. A single pulse of light is emitted. The elapsed time, between emitting and receiving a pulse, is used to recover the object distance

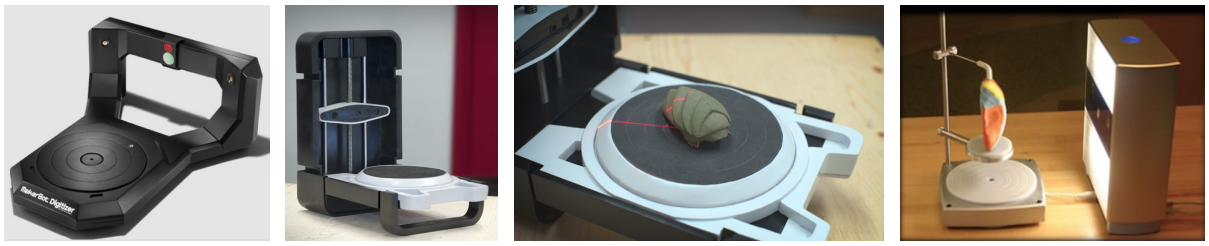

Figure 1.3: Desktop 3D Scanners based on Laser Plane Triangulation. From left to right: MakerBot Digitizer, Matterform Photon, and NextEngine 3D Scanner HD.

(since the speed of light is known). Several economical time-of-flight depth cameras are now commercially available, including Canesta's CANESTAVISION [HARN06] and 3DV's Z-Cam [IY01]. However, the depth resolution and accuracy of such systems (for static scenes) remain below that of slit scanners and structured lighting.

Active imaging is a broad field; a wide variety of additional schemes have been proposed, typically trading system complexity for shape accuracy. As with model-based approaches in passive imaging, several active systems achieve robust reconstruction by making certain simplifying assumptions about the topological and optical properties of the surface. Woodham [Woo89] introduces photometric stereo, allowing smooth surfaces to be recovered by observing their shading under at least three (spatially disparate) point light sources. Hernández et al. [HVB*07] further demonstrate a real-time photometric stereo system using three colored light sources. Similarly, the complex digital projector required for structured lighting can be replaced by one or more printed gratings placed next to the projector and camera. Like shadow moiré, such projection moiré systems create depth-dependent fringes. However, certain ambiguities remain in the reconstruction unless the surface is assumed to be smooth.

Active and passive 3D scanning methods continue to evolve, with recent progress reported annually at various computer graphics and vision conferences, including 3-D Digital Imaging and Modeling (3DIM), SIGGRAPH, Eurographics, CVPR, ECCV, and ICCV. Similar advances are also published in the applied optics communities, typically through various SPIE and OSA journals.

1.2 3D Scanners studied in this Course

This course is grounded in the unifying concept of triangulation. At their core, stereoscopic imaging, slit scanning, and structured lighting all attempt to recover the shape of 3D objects in the same manner. First, the correspondence problem is solved, either by a passive matching algorithm or by an active "space-labeling" approach (e.g., projecting known lines, planes, or other patterns). After establishing correspondences across two or more views (e.g., between a pair of cameras or a single projector-camera pair), triangulation recovers the scene depth. In stereoscopic and multi-view systems, a point is reconstructed by intersecting two or more corresponding lines. In slit scanning and structured lighting systems, a point is recovered by intersecting corresponding lines and planes.

To elucidate the principles of such triangulation-based scanners, this course describes how to construct a classic turntable-based slit scanner, and a structured lighting system. The course also covers methods to register and merge multiple scans, to reconstruct polygon mesh surfaces from multi-scan registered point clouds, and to optimize the reconstructed meshes for various purposes. In all 3D scanner designs, the methods used to calibrate the systems are integral part of

Figure 1.4: Industrial 3D Scanners based on Structured Lighting. From left to right: Breuckmann SmartScan, ATOS CompactScan, and Geomagic Capture.

the design, since they have to be carefully constructed to produce accurate and precise results.

We first study the slit scanner, where a laser line projector iluminates an abject, and a camera captures an image of some or all the illuminated object points. Figure 1.3 shows some commercial desktop 3D scanners based on this method. Image processing techniques are used to detect the pixels corresponding to illuminated points visible by the camera. Ray-plane triangulation equations are used to reconstruct 3D points belonging to the intersection of the plane of laser light and the object. To recover denser sets of 3D points, the laser projector has to be moved while the camera remains static with respect to the object, and the process has to be repeated until a satisfactory number of points has been reconstructed. Alternatively, the object is placed on a linear stage or a turntable, the laser projector is kept static with respect to the camera. The linear stage or turntable is iteratively moved to a new position where an image is captured by the camera. As in the first case, a large number of images must be captured to generate a dense point cloud. In both cases tracking and estimating the motion with precision is required. Computer-controlled motorized linear stages or turntables are normally used for this purpoose. In chapter 4 we describe how to build a low cost turntable-based slit scanner.

Since slit-based scanning systems are line scan systems, they require capturing and processing large numbers of images to produce dense area scans. Structured lighting systems can be used to significantly reduce the number of images (typically by two or more orders of magnitude) required to generate dense 3D scans. Figure 1.4 show some examples of commercial 3D scanners based on structured lighting. In Chapter 5 we describe how to build a low cost structured lighting system using a single LED pico-projector and one or more digital cameras. Many good HD USB web-cameras exist today which can be used for this purpose, but many other options exist today ranging from high end DSLRs to smartphone cameras.

By providing example data sets, open source software, and detailed implementation notes, we hope to enable beginners and hobbyists to replicate our results. We believe the process of building your own 3D scanner to complement your 3D printer will be enjoyable and instructive. Along the way, you'll likely learn a great deal about the practical use of projector-camera systems, hopefully in a manner that supports your own research.

Chapter 2

The Mathematics of Triangulation

This course is primarily concerned with the estimation of 3D shape by illuminating the world with certain known patterns, and observing the illuminated objects with cameras. In this chapter we derive models describing this image formation process, leading to the development of reconstruction equations allowing the recovery of 3D shape by geometric triangulation.

We start by introducing the basic concepts in a coordinate-free fashion, using elementary algebra and the language of analytic geometry (e.g., points, vectors, lines, rays, and planes). Coordinates are introduced later, along with relative coordinate systems, to quantify the process of image formation in cameras and projectors.

2.1 Perspective Projection and the Pinhole Model

A simple and popular geometric model for a camera or a projector is the *pinhole model*, composed of a plane and a point external to the plane (see Figure 2.1). We refer to the plane as the *image plane*, and to the point as the *center of projection*. In a camera, every 3D point (other than the center of projection) determines a unique line passing through the center of projection. If this line is not parallel to the image plane, then it must intersect the image plane in a single *image point*. In mathematics, this mapping from 3D points to 2D image points is referred to as a *perspective projection*. Except for the fact that light traverses this line in the opposite direction, the geometry of a projector can be described with the same model. That is, given a 2D image point in the projector's image plane, there must exist a unique line containing this point and the center of projection (since the center of projection cannot belong to the image plane). In summary, light travels away from a projector (or towards a camera) along the line connecting the 3D scene point with its 2D perspective projection onto the image plane.

2.2 Geometric Representations

Since light moves along straight lines (in a homogeneous medium such as air), we derive 3D reconstruction equations from geometric constructions involving the intersection of lines and planes, or the approximate intersection of pairs of lines (two lines in 3D may not intersect). Our derivations only draw upon elementary algebra and analytic geometry in 3D (e.g., we operate on points, vectors, lines, rays, and planes). We use lower case letters to denote points p and vectors v. All the vectors will be taken as column vectors with real-valued coordinates $v \in \mathbb{R}^3$, which we can also regard as matrices with three rows and one column $v \in \mathbb{R}^{3\times 1}$. The length of a vector v is a scalar $\|v\| \in \mathbb{R}$. We use matrix multiplication notation for the inner product $v_1^t v_2 \in \mathbb{R}$ of two vectors v_1

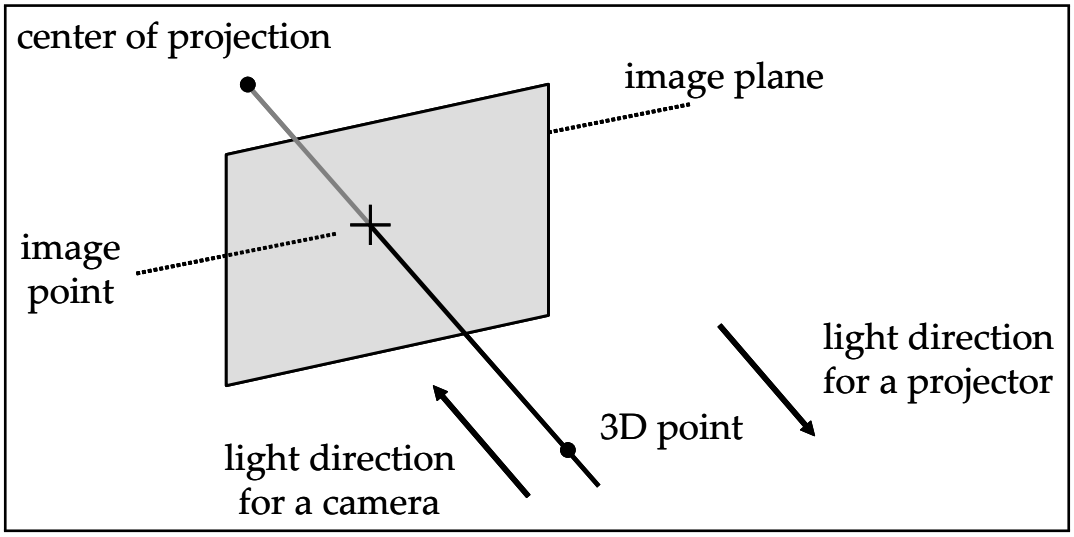

Figure 2.1: Perspective projection under the pinhole model.

and v_2, which is also a scalar. Here $v_1^t \in \mathbb{R}^{1\times 3}$ is a row vector, or a 1×3 matrix, resulting from transposing the column vector v_1. The value of the inner product of the two vectors v_1 and v_2 is equal to $\|v_1\|\|v_2\|\cos(\alpha)$, where α is the angle formed by the two vectors ($0 \leq \alpha \leq 180°$). The $3 \times N$ matrix resulting from concatenating N vectors $v_1, \ldots, v_N$ as columns is denoted $[v_1|\cdots|v_N] \in \mathbb{R}^{3\times N}$. The vector product $v_1 \times v_2 \in \mathbb{R}^3$ of the two vectors v_1 and v_2 is a vector perpendicular to both v_1 and v_2, of length $\|v_1 \times v_2\| = \|v_1\|\,\|v_2\|\,\sin(\alpha)$, and direction determined by the right hand rule (i.e., such that the determinant of the matrix $[v_1|v_2|v_1 \times v_2]$ is non-negative). In particular, two vectors v_1 and v_2 are linearly dependent (i.e., one is a scalar multiple of the other), if and only if the vector product $v_1 \times v_2$ is equal to zero.

2.2.1 Points and Vectors

Since vectors form a vector space, they can be multiplied by scalars and added to each other. Points, on the other hand, do not form a vector space. But vectors and points are related: a point plus a vector $p + v$ is another point, and the difference between two points $q - p$ is a vector. If p is a point, λ is a scalar, and v is a vector, then $q = p + \lambda v$ is another point. In this expression, λv is a vector of length $|\lambda|\,\|v\|$. Multiplying a point by a scalar λp is not defined, but an *affine* combination of N points $\lambda_1 p_1 + \cdots + \lambda_N p_N$, with $\lambda_1 + \cdots + \lambda_N = 1$, is well defined:

$$\lambda_1 p_1 + \cdots + \lambda_N p_N = p_1 + \lambda_2(p_2 - p_1) + \cdots + \lambda_N(p_N - p_1)\ .$$

2.2.2 Parametric Representation of Lines and Rays

A line L can be described by specifying one of its points q and a direction vector v (see Figure 2.2). Any other point p on the line L can be described as the result of adding a scalar multiple λv, of the direction vector v, to the point q (λ can be positive, negative, or zero):

$$L = \{p = q + \lambda v \ :\ \lambda \in \mathbb{R}\}\ . \tag{2.1}$$

This is the *parametric* representation of a line, where the scalar λ is the parameter. Note that this representation is not unique, since q can be replaced by any other point on the line L, and v

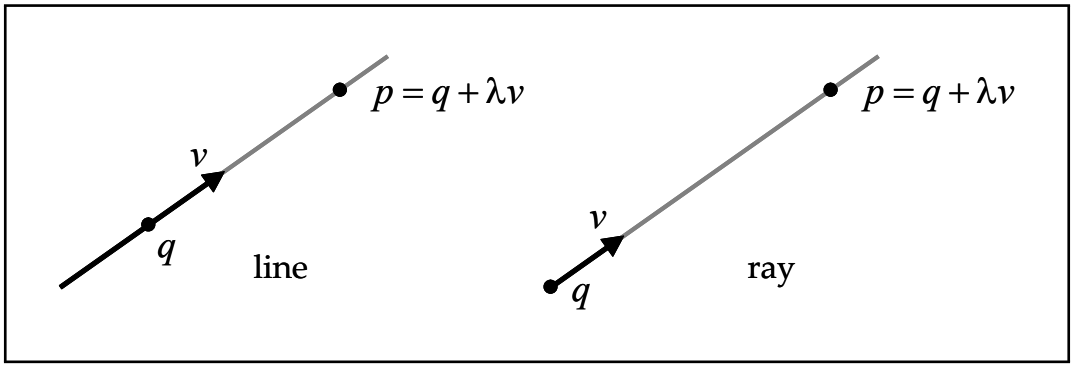

Figure 2.2: Parametric representation of lines and rays.

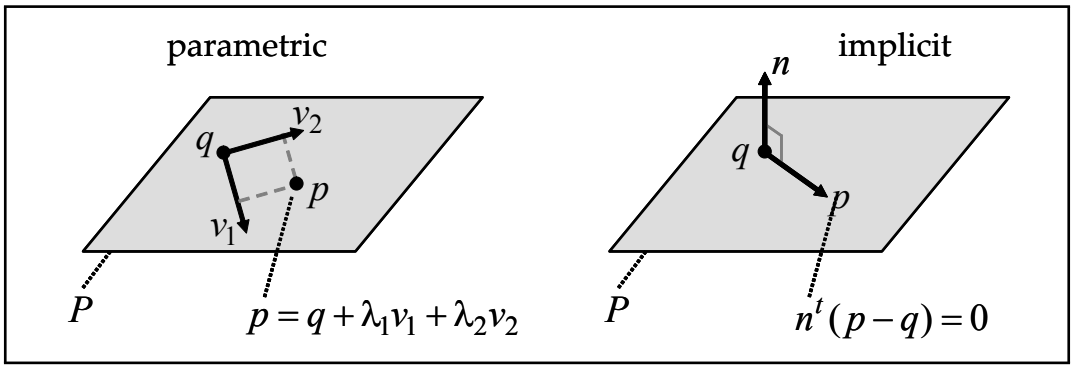

Figure 2.3: Parametric and implicit representations of planes.

can be replaced by any non-zero scalar multiple of v. However, for each choice of q and v, the correspondence between parameters $\lambda \in \mathbb{R}$ and points p on the line L is one-to-one.

A ray is *half* of a line. While in a line the parameter λ can take any value, in a ray it is only allowed to take non-negative values.

$$R = \{p = q + \lambda v \ : \ \lambda \geq 0\}$$

In this case, if the point q is changed, a different ray results. Since it is unique, the point q is called the *origin* of the ray. The direction vector v can be replaced by any *positive* scalar multiple, but not by a negative scalar multiple. Replacing the direction vector v by a negative scalar multiple results in the *opposite* ray. By convention in projectors, light traverses rays along the direction determined by the direction vector. Conversely in cameras, light traverses rays in the direction opposite to the direction vector (i.e., in the direction of decreasing λ).

2.2.3 Parametric Representation of Planes

Similar to how lines are represented in parametric form, a plane P can be described in *parametric* form by specifying one of its points q and two linearly independent direction vectors v_1 and v_2 (see Figure 2.3). Any other point p on the plane P can be described as the result of adding scalar multiples $\lambda_1 v_1$ and $\lambda_2 v_2$ of the two vectors to the point q, as follows.

$$P = \{p = q + \lambda_1 v_1 + \lambda_2 v_2 \ : \ \lambda_1, \lambda_2 \in \mathbb{R}\}$$

As in the case of lines, this representation is not unique. The point q can be replaced by any other point in the plane, and the vectors v_1 and v_2 can be replaced by any other two linearly independent linear combinations of v_1 and v_2.

2.2.4 Implicit Representation of Planes

A plane P can also be described in *implicit* form as the set of zeros of a linear equation in three variables. Geometrically, the plane can be described by one of its points q and a normal vector n. A point p belongs to the plane P if and only if the vectors $p - q$ and n are orthogonal, such that

$$P = \{p \ : \ n^t(p - q) = 0\} \ . \tag{2.2}$$

Again, this representation is not unique. The point q can be replaced by any other point in the plane, and the normal vector n by any non-zero scalar multiple λn.

To convert from the parametric to the implicit representation, we can take the normal vector $n = v_1 \times v_2$ as the vector product of the two basis vectors v_1 and v_2. To convert from implicit to parametric, we need to find two linearly independent vectors v_1 and v_2 orthogonal to the normal vector n. In fact, it is sufficient to find one vector v_1 orthogonal to n. The second vector can be defined as $v_2 = n \times v_1$. In both cases, the same point q from one representation can be used in the other.

2.2.5 Implicit Representation of Lines

A line L can also be described in *implicit* form as the intersection of two planes, both represented in implicit form, such that

$$L = \{p \ : \ n_1^t(p - q) = n_2^t(p - q) = 0\}, \tag{2.3}$$

where the two normal vectors n_1 and n_2 are linearly independent (if n_1 an n_2 are linearly dependent, rather than a line, the two equations describe the same plane). Note that when n_1 and n_2 are linearly independent, the two implicit representations for the planes can be defined with respect to a common point belonging to both planes, rather than to two different points. Since a line can be described as the intersection of many different pairs of planes, this representation is not unique. The point q can be replaced by any other point belonging to the intersection of the two planes, and the two normal vectors can be replaced by any other pair of linearly independent linear combinations of the two vectors.

To convert from the parametric representation of Equation 2.1 to the implicit representation of Equation 2.3, one needs to find two linearly independent vectors n_1 and n_2 orthogonal to the direction vector v. One way to do so is to first find one non-zero vector n_1 orthogonal to v, and then take n_2 as the vector product $n_2 = v \times n_1$ of v and n_1. To convert from implicit to parametric, one needs to find a non-zero vector v orthogonal to both normal vectors n_1 and n_2. The vector product $v = n_1 \times n_2$ is one such vector, and any other is a scalar multiple of it.

2.3 Reconstruction by Triangulation

As will be discussed in Chapters **??** and 5, it is common for projected illumination patterns to contain identifiable lines or points. Under the pinhole projector model, a projected line creates a plane of light (the unique plane containing the line on the image plane and the center of projection), and

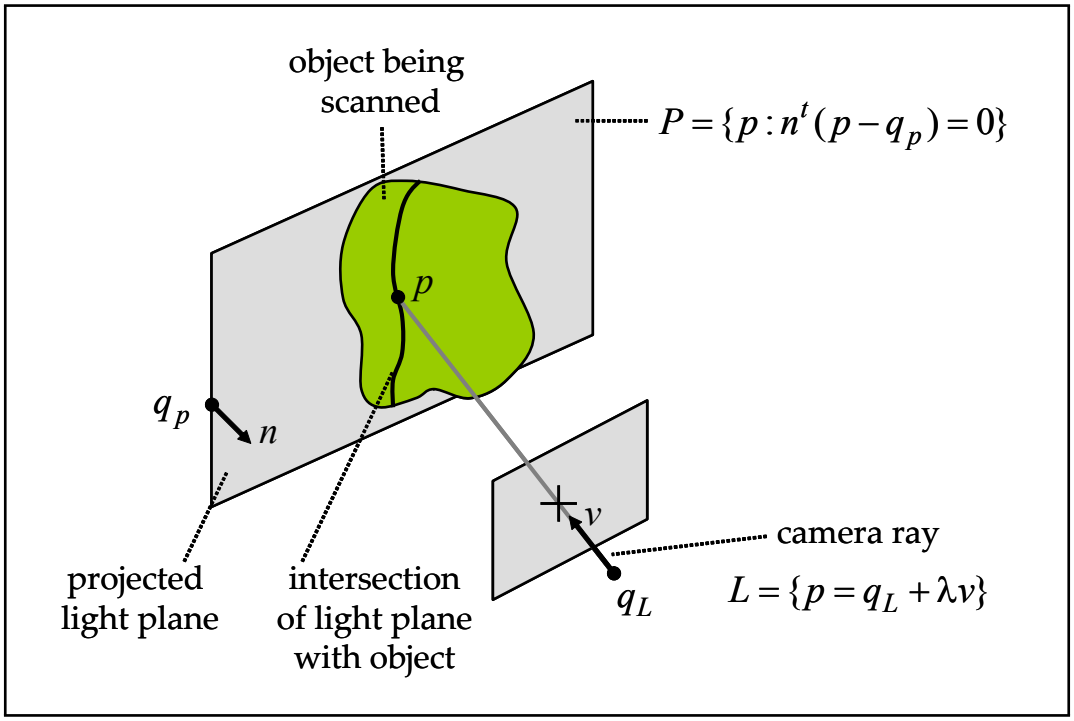

Figure 2.4: Triangulation by line-plane intersection.

a projected point creates a ray of light (the unique line containing the image point and the center of projection).

While the intersection of a ray of light with the object being scanned can be considered as a single illuminated point, the intersection of a plane of light with the object generally contains many illuminated curved segments (see Figure 1.2). Each of these segments is composed of many illuminated points. A single illuminated point, visible to the camera, defines a camera ray. For now, we assume that the locations and orientations of projector and camera are known with respect to the global coordinate system (with procedures for estimating these quantities covered in Chapter 3). Under this assumption, the equations of projected planes and rays, as well as the equations of camera rays corresponding to illuminated points, are defined by parameters which can be measured. From these measurements, the location of illuminated points can be recovered by intersecting the planes or rays of light with the camera rays corresponding to the illuminated points. Through such procedures the depth ambiguity introduced by pinhole projection can be eliminated, allowing recovery of a 3D surface model.

2.3.1 Line-Plane Intersection

Computing the intersection of a line and a plane is straightforward when the line is represented in parametric form

$$L = \{p = q_L + \lambda v \ : \ \lambda \in \mathbb{R}\},$$

and the plane is represented in implicit form

$$P = \{p \ : \ n^t(p - q_P) = 0\} \ .$$

Note that the line and the plane may not intersect, in which case we say that the line and the plane are *parallel*. This is the case if the vectors v and n are orthogonal $n^t v = 0$. The vectors v

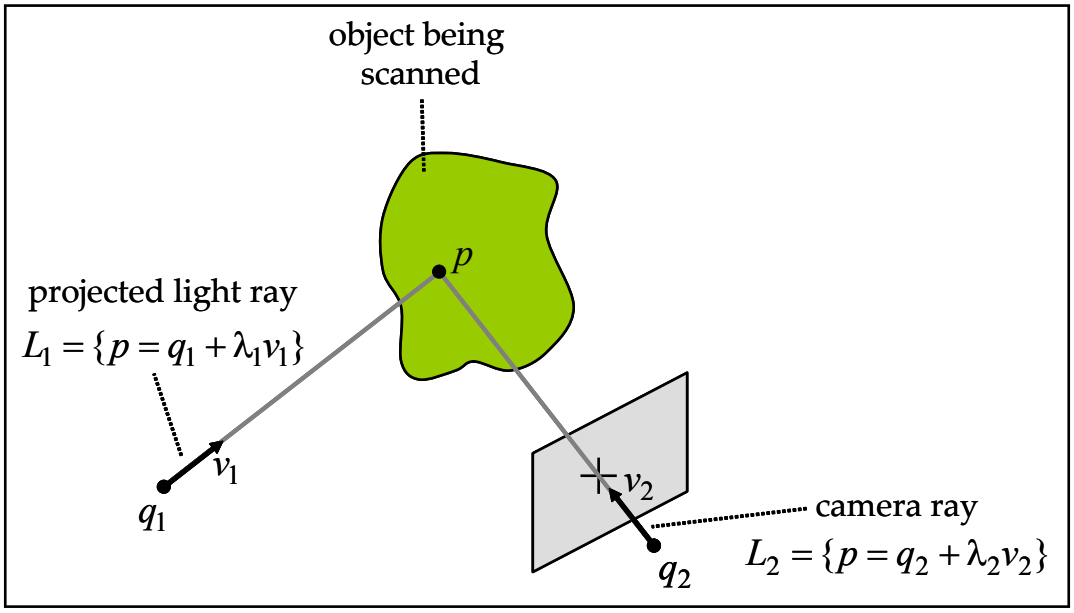

Figure 2.5: Triangulation by line-line intersection.

and n are also orthogonal when the line L is contained in the plane P. Whether or not the point q_L belongs to the plane P differentiates one case from the other. If the vectors v and n are not orthogonal $n^t v \neq 0$, then the intersection of the line and the plane contains exactly one point p. Since this point belongs to the line, it can be written as $p = q_L + \lambda v$, for a value λ which we need to determine. Since the point also belongs to the plane, the value λ must satisfy the linear equation

$$n^t(p - q_p) = n^t(\lambda v + q_L - q_p) = 0 \ ,$$

or equivalently

$$\lambda = \frac{n^t(q_P - q_L)}{n^t v} \ . \tag{2.4}$$

Since we have assumed that the line and the plane are not parallel (i.e., by checking that $n^t v \neq 0$ beforehand), this expression is well defined. A geometric interpretation of line-plane intersection is provided in Figure 2.4.

2.3.2 Line-Line Intersection

We consider here the intersection of two arbitrary lines L_1 and L_2, as shown in Figure 2.5.

$$L_1 = \{p = q_1 + \lambda_1 v_1 \ : \ \lambda_1 \in \mathbb{R}\} \quad \text{and} \quad L_2 = \{p = q_2 + \lambda_2 v_2 \ : \ \lambda_2 \in \mathbb{R}\}$$

Let us first identify the special cases. The vectors v_1 and v_2 can be linearly dependent (i.e., if one is a scalar multiple of the other) or linearly independent.

The two lines are parallel if the vectors v_1 and v_2 are linearly dependent. If, in addition, the vector $q_2 - q_1$ can also be written as a scalar multiple of v_1 or v_2, then the lines are identical. Of course, if the lines are parallel but not identical, they do not intersect.

If v_1 and v_2 are linearly independent, the two lines may or may not intersect. If the two lines intersect, the intersection contains a single point. The necessary and sufficient condition for two

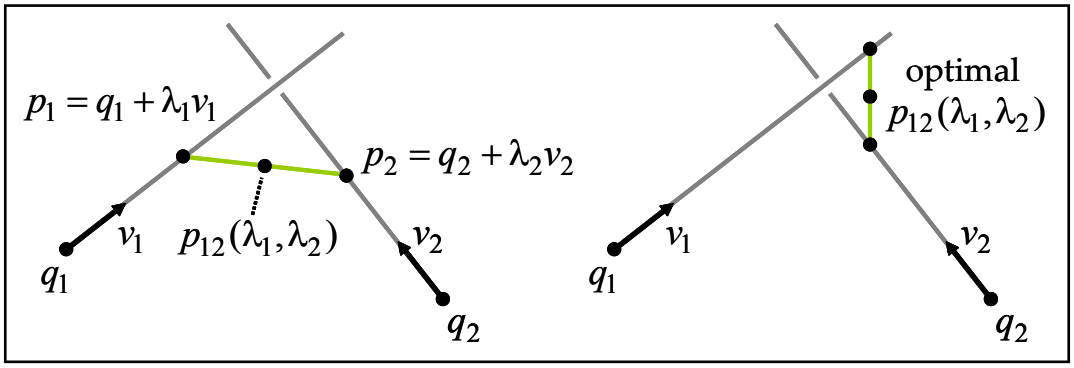

Figure 2.6: The midpoint $p_{12}(\lambda_1, \lambda_2)$ for arbitrary values (left) of λ_1, λ_2 and for the optimal values (right).

lines to intersect, when v_1 and v_2 are linearly independent, is that scalar values λ_1 and λ_2 exist so that

$$q_1 + \lambda_1 v_1 = q_2 + \lambda_2 v_2,$$

or equivalently so that the vector $q_2 - q_1$ is linearly dependent on v_1 and v_2.

Since two lines may not intersect, we define the *approximate intersection* as the point which is *closest* to the two lines. More precisely, whether two lines intersect or not, we define the approximate intersection as the point p which minimizes the sum of the square distances to both lines

$$\phi(p, \lambda_1, \lambda_2) = \|q_1 + \lambda_1 v_1 - p\|^2 + \|q_2 + \lambda_2 v_2 - p\|^2 \ .$$

As before, we assume v_1 and v_2 are linearly independent, such the approximate intersection is a unique point.

To prove that the previous statement is true, and to determine the value of p, we follow an algebraic approach. The function $\phi(p, \lambda_1, \lambda_2)$ is a quadratic non-negative definite function of five variables, the three coordinates of the point p and the two scalars λ_1 and λ_2.

We first reduce the problem to the minimization of a different quadratic non-negative definite function of only two variables λ_1 and λ_2. Let $p_1 = q_1 + \lambda_1 v_1$ be a point on the line L_1, and let $p_2 = q_2 + \lambda_2 v_2$ be a point on the line L_2. Define the midpoint p_{12}, of the line segment joining $p1$ and $p2$, as

$$p_{12} = p_1 + \frac{1}{2}(p_2 - p_1) = p_2 + \frac{1}{2}(p_1 - p_2) \ .$$

A necessary condition for the minimizer $(p, \lambda_1, \lambda_2)$ of ϕ is that the partial derivatives of ϕ, with respect to the five variables, all vanish at the minimizer. In particular, the three derivatives with respect to the coordinates of the point p must vanish

$$\frac{\partial \phi}{\partial p} = (p - p_1) + (p - p_2) = 0 \ ,$$

or equivalently, it is necessary for the minimizer point p to be the midpoint p_{12} of the segment joining p_1 and p_2 (see Figure 2.6).

As a result, the problem reduces to the minimization of the square distance from a point p_1 on line L_1 to a point p_2 on line L_2. Practically, we must now minimize the quadratic non-negative definite function of two variables

$$\psi(\lambda_1, \lambda_2) = 2\phi(p_{12}, \lambda_1, \lambda_2) = \|(q_2 + \lambda_2 v_2) - (q_1 + \lambda_1 v_1)\|^2 \ .$$

Note that it is still necessary for the two partial derivatives of ψ, with respect to λ_1 and λ_2, to be equal to zero at the minimum, as follows.

$$\frac{\partial \psi}{\partial \lambda_1} = v_1^t(\lambda_1 v_1 - \lambda_2 v_2 + q_1 - q_2) = \lambda_1 \|v_1\|^2 - \lambda_2 v_1^t v_2 + v_1^t(q_1 - q_2) = 0$$

$$\frac{\partial \psi}{\partial \lambda_2} = v_2^t(\lambda_2 v_2 - \lambda_1 v_1 + q_2 - q_1) = \lambda_2 \|v_2\|^2 - \lambda_2 v_2^t v_1 + v_2^t(q_2 - q_1) = 0$$

These provide two linear equations in λ_1 and λ_2, which can be concisely expressed in matrix form as

$$\begin{pmatrix} \|v_1\|^2 & -v_1^t v_2 \\ -v_2^t v_1 & \|v_2\|^2 \end{pmatrix} \begin{pmatrix} \lambda_1 \\ \lambda_2 \end{pmatrix} = \begin{pmatrix} v_1^t(q_2 - q_1) \\ v_2^t(q_1 - q_2) \end{pmatrix} .$$

It follows from the linear independence of v_1 and v_2 that the 2×2 matrix on the left hand side is non-singular. As a result, the unique solution to the linear system is given by

$$\begin{pmatrix} \lambda_1 \\ \lambda_2 \end{pmatrix} = \begin{pmatrix} \|v_1\|^2 & -v_1^t v_2 \\ -v_2^t v_1 & \|v_2\|^2 \end{pmatrix}^{-1} \begin{pmatrix} v_1^t(q_2 - q_1) \\ v_2^t(q_1 - q_2) \end{pmatrix}$$

or equivalently

$$\begin{pmatrix} \lambda_1 \\ \lambda_2 \end{pmatrix} = \frac{1}{\|v_1\|^2\|v_2\|^2 - (v_1^t v_2)^2} \begin{pmatrix} \|v_2\|^2 & v_1^t v_2 \\ v_2^t v_1 & \|v_1\|^2 \end{pmatrix} \begin{pmatrix} v_1^t(q_2 - q_1) \\ v_2^t(q_1 - q_2) \end{pmatrix} . \tag{2.5}$$

In conclusion, the approximate intersection p can be obtained from the value of either λ_1 or λ_2 provided by these expressions.

2.4 Coordinate Systems

So far we have presented a coordinate-free description of triangulation. In practice, however, image measurements are recorded in discrete pixel units. In this section we incorporate such coordinates into our prior equations, as well as document the various coordinate systems involved.

2.4.1 Image Coordinates and the Pinhole Camera

Consider a pinhole model with center of projection o and image plane $P = \{p = q + u^1 v_1 + u^2 v_2 : u^1, u^2 \in \mathbb{R}\}$. Any 3D point p, not necessarily on the image plane, has coordinates $(p^1, p^2, p^3)^t$ relative to the origin of the world coordinate system. On the image plane, the point q and vectors v_1 and v_2 define a local coordinate system. The image coordinates of a point $p = q + u^1 v_1 + u^2 v_2$ are the parameters u^1 and u^2, which can be written as a 3D vector $u = (u^1, u^2, 1)$. Using this notation point p is expressed as

$$\begin{pmatrix} p^1 \\ p^2 \\ p^3 \end{pmatrix} = [v_1 | v_2 | q] \begin{pmatrix} u^1 \\ u^2 \\ 1 \end{pmatrix} .$$

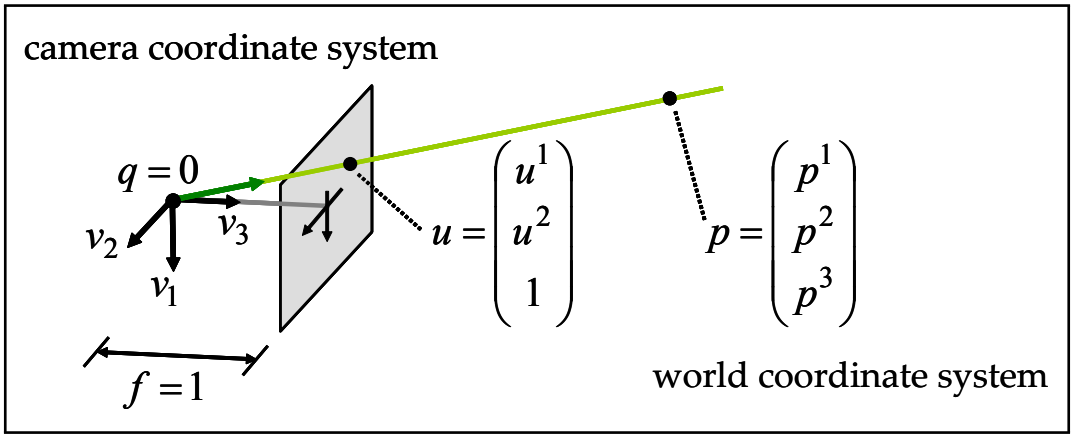

Figure 2.7: The ideal pinhole camera.

2.4.2 The Ideal Pinhole Camera

In the *ideal pinhole camera* shown in Figure 2.7, the center of projection o is at the origin of the world coordinate system, with coordinates $(0,0,0)^t$, and the point q and the vectors v_1 and v_2 are defined as

$$[v_1|v_2|q] = \begin{pmatrix} 1 & 0 & 0 \\ 0 & 1 & 0 \\ 0 & 0 & 1 \end{pmatrix} .$$

Note that not every 3D point has a projection on the image plane. Points without a projection are contained in a plane parallel to the image passing through the center of projection. An arbitrary 3D point p with coordinates $(p^1, p^2, p^3)^t$ belongs to this plane if $p^3 = 0$, otherwise it projects onto an image point with the following coordinates.

$$\begin{aligned} u^1 &= p^1/p^3 \\ u^2 &= p^2/p^3 \end{aligned}$$

There are other descriptions for the relation between the coordinates of a point and the image coordinates of its projection; for example, the projection of a 3D point p with coordinates $(p^1, p^2, p^3)^t$ has image coordinates $u = (u^1, u^2, 1)$ if, for some scalar $\lambda \neq 0$, we can write

$$\lambda \begin{pmatrix} u^1 \\ u^2 \\ 1 \end{pmatrix} = \begin{pmatrix} p^1 \\ p^2 \\ p^3 \end{pmatrix} . \tag{2.6}$$

2.4.3 The General Pinhole Camera

The center of a general pinhole camera is not necessarily placed at the origin of the world coordinate system and may be arbitrarily oriented. However, it does have a *camera coordinate system* attached to the camera, in addition to the *world coordinate system* (see Figure 2.8). A 3D point p has world coordinates described by the vector $p_W = (p^1_W, p^2_W, p^3_W)^t$ and camera coordinates described by the vector $p_C = (p^1_C, p^2_C, p^3_C)^t$. These two vectors are related by a rigid body transformation specified by a translation vector $T \in \mathbb{R}^3$ and a rotation matrix $R \in \mathbb{R}^{3\times 3}$, such that

$$p_C = R\, p_W + T .$$

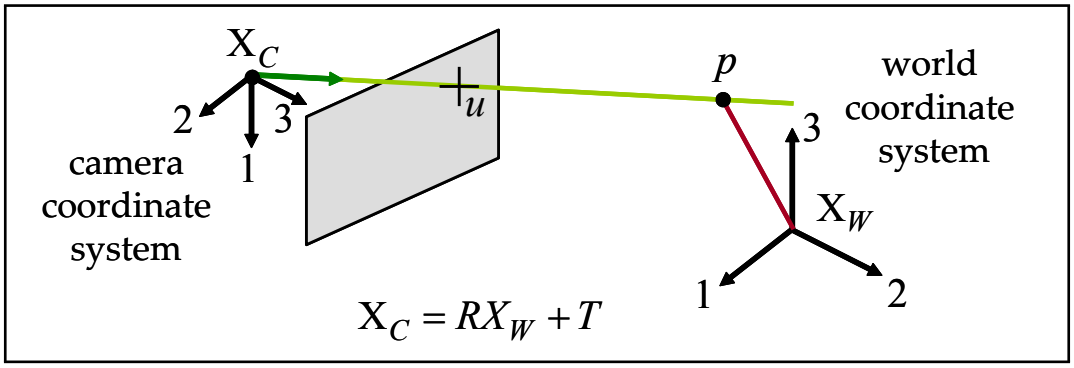

Figure 2.8: The general pinhole model.

In camera coordinates, the relation between the 3D point coordinates and the 2D image coordinates of the projection is described by the ideal pinhole camera projection (i.e., Equation 2.6), with $\lambda u = p_C$. In world coordinates this relation becomes

$$\lambda\, u = R\, p_W + T\ . \tag{2.7}$$

The parameters (R, T), which are referred to as the *extrinsic parameters* of the camera, describe the location and orientation of the camera with respect to the world coordinate system.

Equation 2.7 assumes that the unit of measurement of lengths on the image plane is the same as for world coordinates, that the distance from the center of projection to the image plane is equal to one unit of length, and that the origin of the image coordinate system has image coordinates $u^1 = 0$ and $u^2 = 0$. None of these assumptions hold in practice. For example, lengths on the image plane are measured in pixel units, and in meters or inches for world coordinates, the distance from the center of projection to the image plane can be arbitrary, and the origin of the image coordinates is usually on the upper left corner of the image. In addition, the image plane may be tilted with respect to the ideal image plane. To compensate for these limitations of the current model, a matrix $K \in \mathbb{R}^{3\times 3}$ is introduced in the projection equations to describe *intrinsic parameters* as follows.

$$\lambda\, u = K(R\, p_W + T) \tag{2.8}$$

The matrix K has the following form

$$K = \begin{pmatrix} f\, s_1 & f\, s_\theta & o^1 \\ 0 & f\, s_2 & o^2 \\ 0 & 0 & 1 \end{pmatrix}\ ,$$

where f is the *focal length* (i.e., the distance between the center of projection and the image plane). The parameters s_1 and s_2 are the first and second coordinate scale parameters, respectively. Note that such scale parameters are required since some cameras have non-square pixels. The parameter s_θ is used to compensate for a tilted image plane. Finally, $(o^1, o^2)^t$ are the image coordinates of the intersection of the vertical line in camera coordinates with the image plane. This point is called the *image center* or *principal point*. Note that all intrinsic parameters embodied in K are independent of the camera pose. They describe physical properties related to the mechanical and optical design of the camera. Since in general they do not change, the matrix K can be estimated once through a calibration procedure and stored (as will be described in the following chapter).

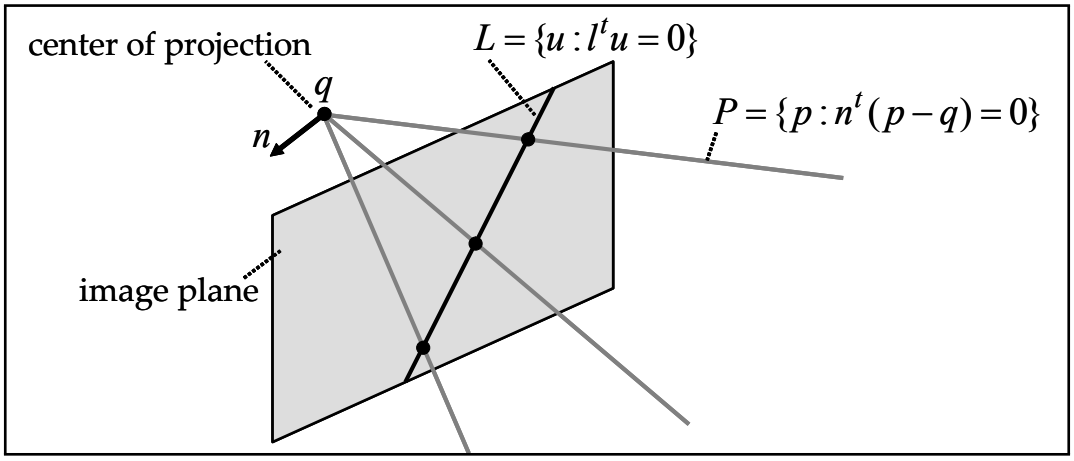

Figure 2.9: The plane defined by an image line and the center of projection.

Afterwards, image plane measurements in pixel units can immediately be "normalized", by multiplying the measured image coordinate vector by K^{-1}, so that the relation between a 3D point in world coordinates and 2D image coordinates is described by Equation 2.7.

Real cameras also display non-linear lens distortion, which is also considered intrinsic. Lens distortion compensation must be performed prior to the normalization described above. We will discuss appropriate lens distortion models in Chapter 3.

2.4.4 Lines from Image Points

As shown in Figure 2.9, an image point with coordinates $u = (u^1, u^2, 1)^t$ defines a unique line containing this point and the center of projection. The challenge is to find the parametric equation of this line, as $L = \{p = q + \lambda\, v \,:\, \lambda \in \mathbb{R}\}$. Since this line must contain the center of projection, the projection of all the points it spans must have the same image coordinates. If p_W is the vector of world coordinates for a point contained in this line, then world coordinates and image coordinates are related by Equation 2.7 such that $\lambda\, u = R\, p_W + T$. Since R is a rotation matrix, we have $R^{-1} = R^t$ and we can rewrite the projection equation as

$$p_W = (-R^t T) + \lambda\, (R^t u)\ .$$

In conclusion, the line we are looking for is described by the point q with world coordinates $q_W = -R^t T$, which is the center of projection, and the vector v with world coordinates $v_W = R^t u$.

2.4.5 Planes from Image Lines

A straight line on the image plane can be described in either parametric or implicit form, both expressed in image coordinates. Let us first consider the implicit case. A line on the image plane is described by one implicit equation of the image coordinates

$$L = \{u : l^t u = l^1 u^1 + l^2 u^2 + l^3 = 0\}\ ,$$

where $l = (l^1, l^2, l^3)^t$ is a vector with $l^1 \neq 0$ or $l^2 \neq 0$. Using active illumination, projector patterns containing vertical and horizontal lines are common. Thus, the implicit equation of an horizontal line is

$$L_H = \{u : l^t u = u^2 - \nu = 0\}\ ,$$

where ν is the second coordinate of a point on the line. In this case we can take $l = (0, 1, -\nu)^t$. Similarly, the implicit equation of a vertical line is

$$L_V = \{u : l^t u = u^1 - \nu = 0\} ,$$

where ν is now the first coordinate of a point on the line. In this case we can take $l = (1, 0, -\nu)^t$. There is a unique plane P containing this line L and the center of projection. For each image point with image coordinates u on the line L, the line containing this point and the center of projection is contained in P. Let p be a point on the plane P with world coordinates p_W projecting onto an image point with image coordinates u. Since these two vectors of coordinates satisfy Equation 2.7, for which $\lambda\, u = R\, p_W + T$, and the vector u satisfies the implicit equation defining the line L, we have

$$0 = \lambda l^t u = l^t (R\, p_W + T) = (R^t l)^t \, (p_W - (-R^t T)) .$$

In conclusion, the implicit representation of plane P, corresponding to Equation 2.2 for which $P = \{p : n^t (p - q) = 0\}$, can be obtained with n being the vector with world coordinates $n_W = R^t l$ and q the point with world coordinates $q_W = -R^t T$, which is the center of projection.

Chapter 3

Camera and Projector Calibration

Triangulation is a deceptively simple concept, simply involving the pairwise intersection of 3D lines and planes. Practically, however, one must carefully calibrate the various cameras and projectors so the equations of these geometric primitives can be recovered from image measurements. In this chapter we lead the reader through the construction and calibration of a basic projector-camera system. Through this example, we examine how freely-available calibration packages, emerging from the computer vision community, can be leveraged in your own projects. While touching on the basic concepts of the underlying algorithms, our primarily goal is to help beginners overcome the "calibration hurdle".

In Section 3.1 we describe how to select, control, and calibrate a digital camera suitable for 3D scanning. The general pinhole camera model presented in Chapter 2 is extended to address lens distortion. A simple calibration procedure using printed checkerboard patterns is presented, following the established method of Zhang [Zha00]. Typical calibration results, obtained for the cameras used in Chapters 4 and 5, are provided as a reference.

Well-documented, freely-available camera calibration tools have been known for several years now, but projector calibration received broader attention just recently with the increasing interest in building white-light scanners. In Section 3.2, we describe an open-source Projector-Camera Calibration tool [MT12] which extends the printed checkerboard method to calibrated both projector and camera. We conclude by reviewing calibration results for the structured light projector used in Chapter 5.

3.1 Camera Calibration

In this section we describe both the theory and practice of camera calibration. We begin by briefly considering which cameras are best suited for building your own 3D scanner. We then present the widely-used calibration method originally proposed by Zhang [Zha00]. Finally, we provide step-by-step directions on how to use a freely-available MATLAB-based implementation of Zhang's method.

3.1.1 Camera selection and interfaces

Selection of the "best" camera depends on your budget, project goals, and preferred development environment. Probably the most confusing part for the inexperienced user is the variety of camera buses available raging from the traditional IEEE 1394 FireWire, the more common USB 2.0 and 3.0, to Camera Link and GigE Vision buses. Selection of the right bus must begin considering the throughput requirement for the application, the chosen bus must be able to transfer

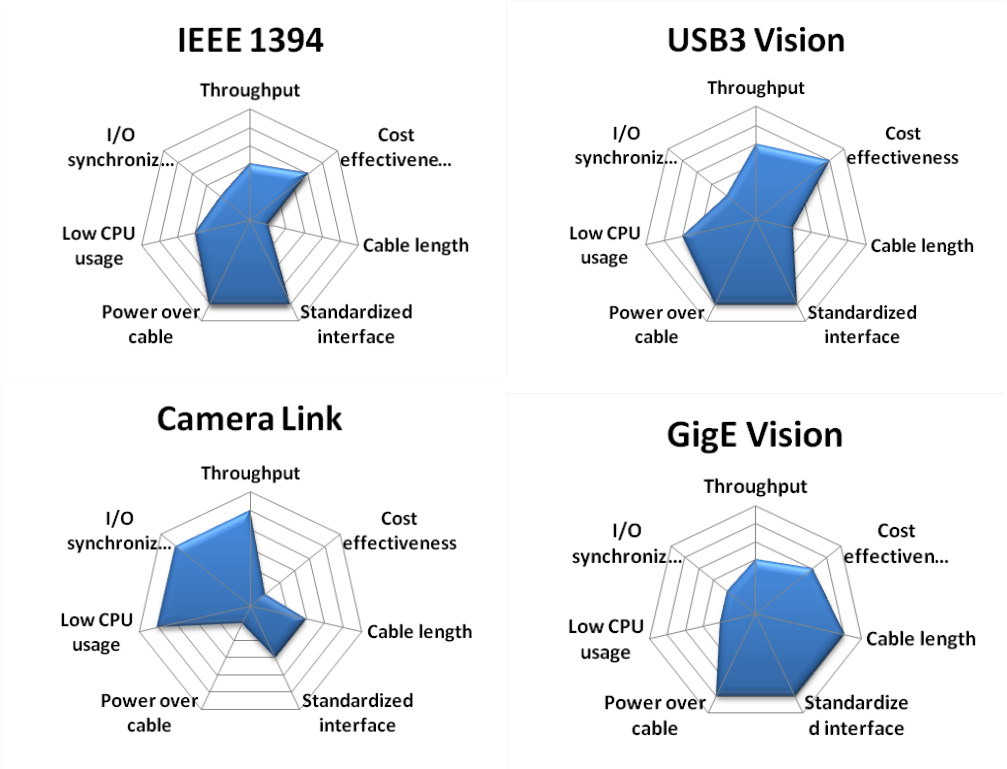

Figure 3.1: Vision camera buses comparison (Source: National Instruments white paper. [Na13]).

images at the required framerate. Other aspects to consider are camera cable length, effective cost, and whether hardware synchronization triggers will be used. These characteristics are compared graphically in Figure 3.1. We refer the user interested in learning more about vision camera buses to [Na13]. Besides camera buses, other aspects to consider when choosing a camera are their sensor specifications (size, resolution, color or grayscale) and whether they have a fixed lens or a lens mount. When choosing lenses the focal length must be considered, which determines—together with sensor size—the effective field of view of the camera. In this course we recommend standard USB cameras because they are low cost and they do not require special hardware or software, this come at a price of a low throughput and limited control and customization. Specifically, we will use a Logitech C920 which can capture images with a resolution of 1920×1080, Figure 3.2(a). Although more expensive, we also recommend cameras from Point Grey Research. The camera interface provided by this vendor is particularly useful if you plan on developing more advanced scanners than those presented here, and particularly if you need access to raw sensor data. As a point of reference, we have tested a Point Grey GRAS-20S4M/C Grasshopper, Figure 3.2(b), at a resolution of 1600×1200 up to 30 Hz [Poi].

At the time of writing, the accompanying software for this course was primarily written in MATLAB. If readers wish to collect their own data sets using our software, we recommend obtaining a camera supported by the Image Acquisition Toolbox for MATLAB [Mat]. Note that this toolbox supports products from a variety of vendors, as well as any DCAM-compatible FireWire camera or webcam with a Windows Driver Model (WDM) or Video for Windows (VFW) driver. For FireWire cameras the toolbox uses the CMU DCAM driver [CMU]. Alternatively, we encourage users to write their own image acquisition tools using standard libraries as OpenCV [Ope] or SimpleCV [Sim]. OpenCV has a variety of ready-to-use computer vision algorithms—such as

(a) Logitech HD Pro Webcam C920

(b) Point Grey Grasshopper IEEE-1394b (without lens)

Figure 3.2: Recommended cameras for course projects.

camera calibration—optimized for several platforms, including Windows, Mac OS X, Linux, and Android; which can be accessed in C++, Java, and Python. SimpleCV is a high-level framework, with a faster learning curve, for developing computer vision software in Python.

3.1.2 Calibration Methods and Software

Camera Calibration Methods

Camera calibration requires estimating the parameters of the general pinhole model presented in Section 2.4.3. This includes the intrinsic parameters, being focal length, principal point, and the scale factors, as well as the extrinsic parameters, defined by a rotation matrix and translation vector mapping between the world and camera coordinate systems. In total, 11 parameters (5 intrinsic and 6 extrinsic) must be estimated from a calibration sequence. In practice, a lens distortion model must be estimated as well. We recommend the reader review [HZ04, MSKS05] for an in-depth description of camera models and calibration methods.

At a basic level, camera calibration requires recording a sequence of images of a calibration object, composed of a unique set of distinguishable features with known 3D displacements. Thus, each image of the calibration object provides a set of 2D-to-3D correspondences, mapping image coordinates to scene points. Naïvely, one would simply need to optimize over the set of 11 camera model parameters so that the set of 2D-to-3D correspondences are correctly predicted (i.e., the projection of each known 3D model feature is close to its measured image coordinates).

Many methods have been proposed over the years to solve for the camera parameters given such correspondences. In particular, the factorized approach originally proposed Zhang [Zha00] is widely-adopted in most community-developed tools. In this method, a planar checkerboard pattern is observed in two or more orientations (see Figure 3.3). From this sequence, the intrinsic parameters can be separately solved. Afterwards, a single view of a checkerboard can be used to solve for the extrinsic parameters. Given the relative ease of printing 2D patterns, this method is commonly used in computer graphics and vision publications.

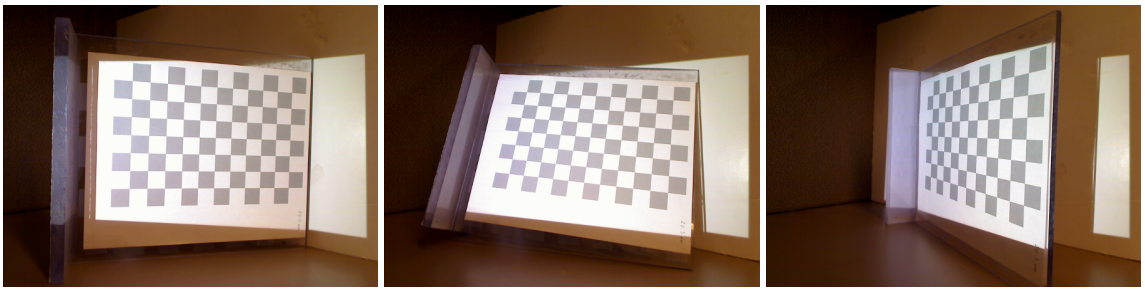

Figure 3.3: Camera calibration images containing a checkerboard with different orientations throughout the scene.

Recommended Software

A comprehensive list of calibration software is maintained by Bouguet on the toolbox website[1]. We recommend course attendees use the MATLAB toolbox. Otherwise, OpenCV replicates many of its functionalities, while supporting multiple platforms. A CALTag [AHH10] checkerboard and software is yet another alternative. CALTag patterns are designed to provide features even if some checkerboard regions are occluded, we wil use this feature in Section 4.2 to calibrate a turntable.

Although calibrating a small number of cameras using these tools is straightforward, calibrating a large network of cameras is a relatively challenging problem. If your projects lead you in this direction, we suggest to consider the self-calibration toolbox [SMP05], or a new toolbox based on a feature-descriptor pattern [LHKP13] instead. The former, rather than using multiple views of a planar calibration object, detects a standard laser point being translated through the working volume and correspondences between the cameras are automatically determined from the tracked projection of the pointer in each image. The latter, creates a pattern using multiple SIFT/SURF features at different scales which can be automatically detected. In contrast with the checkerboard approach, features can be uniquely identified—similar to CALTag cells—even when partial views of the pattern are available due to limited intersection of the multiple cameras field of view.

3.1.3 Calibration Procedure

In this section we describe, step-by-step, how to calibrate your camera using the Camera Calibration Toolbox for MATLAB. We also recommend reviewing the detailed documentation and examples provided on the toolbox website. Specifically, new users should work through the first calibration example and familiarize themselves with the description of model parameters (which differ slightly from the notation used in these notes).

Begin by installing the toolbox, available for download at the software website[1]. Next, construct a checkerboard target. Note that the toolbox comes with a sample checkerboard image; print this image and affix it to a rigid object, such as piece of cardboard or textbook cover. Record a series of 10–20 images of the checkerboard, varying its position and pose between exposures. Try to collect images where the checkerboard is visible throughout the image, and specially, the checkerboard must cover a large region in each image.

Using the toolbox is relatively straightforward. Begin by adding the toolbox to your MATLAB path by selecting "File → Set Path...". Next, change the current working directory to one containing your calibration images (or one of our test sequences). Type `calib` at the MATLAB prompt

[1] http://www.vision.caltech.edu/bouguetj/calib_doc/

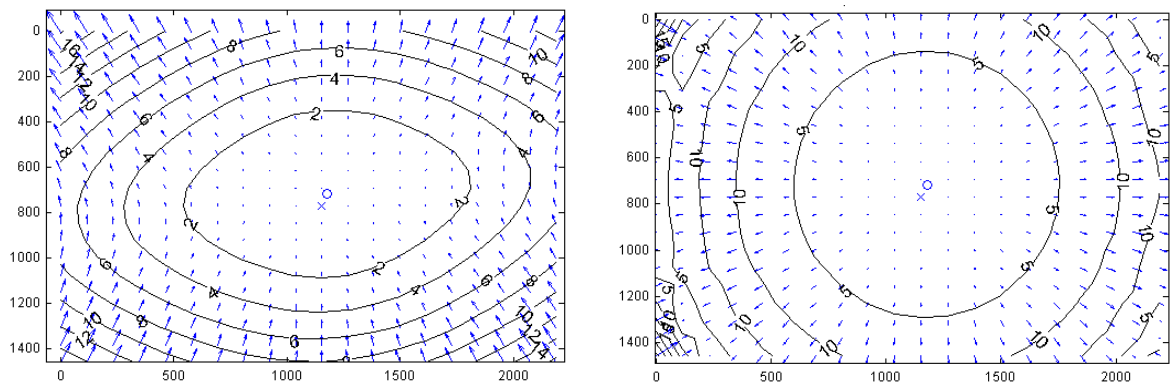

(a) Tangential Component (b) Radial Component

Figure 3.4: Camera calibration distortion model. Sample distortion model of the Logitech C920 Webcam used in the Laser Stripe Scanner of Chapter 4. The plots show the center of distortion $\times$ at the principal point, and the amount of distortion in pixel units increasing towards the border.

to start. Since we are only using a few images, select "Standard (all the images are stored in memory)" when prompted. To load the images, select "Image names" and press return, then "j" (JPEG images). Now select "Extract grid corners", pass through the prompts without entering any options, and then follow the on-screen directions. The default checkerboard has 30mm$\times$30mm squares but the actual dimensions vary from printer to printer, you should measure your own checkerboard and use those values instead. Always skip any prompts that appear, unless you are more familiar with the toolbox options. Once you have finished selecting corners, choose "Calibration", which will run one pass though the calibration algorithm. Next, choose "Analyze error". Left-click on any outliers you observe, then right-click to continue. Repeat the corner selection and calibration steps for any remaining outliers (this is a manually-assisted form of bundle adjustment). Once you have an evenly-distributed set of reprojection errors, select "Recomp. corners" and finally "Calibration". To save your intrinsic calibration, select "Save".

From the previous step you now have an estimate of how pixels can be converted into normalized coordinates (and subsequently optical rays in world coordinates, originating at the camera center). Note that this procedure estimates both the intrinsic and extrinsic parameters, as well as the parameters of a lens distortion model. Typical calibration results, illustrating the lens distortion model is shown in Figure 3.4. The actual result of the calibration is displayed below as reference.

Logitech C920 Webcam sample calibration result:

```
Focal Length:          fc = [ 1642.17076 1642.83775 ]
                       +/- [    2.91675    1.85405 ]
Principal point:       cc = [ 1176.14705  714.90826 ]
                       +/- [    2.63232    3.58792 ]
Skew: alpha_c = [ 0.00000 ] +/- [ 0.00000  ]
   => angle of pixel axes = 90.0000 +/- 0.0000 degrees
Distortion:
   kc = [ 0.09059 -0.16979 -0.00796 -0.00078 0.00000 ]
    +/- [ 0.00333  0.01042  0.00051  0.00065 0.00000 ]
Pixel error:          err = [     0.25706    0.27527 ]
```

Figure 3.5: Recommended projectors for course projects: (Left) Dell M110 DLP Pico Projector, (Right) Optoma PK320 Pico Pocket Projector.

3.2 Projector Calibration

We now turn our attention to projector calibration. Following the conclusions of Chapter 2, we model the projector as an inverse camera (i.e., one in which light travels in the opposite direction from usual). Under this model, calibration proceeds in a similar manner as with cameras, where correspondences between 3D points world coordinates and projector pixel locations are used to estimate the pinhole model parameters. For camera calibration, we use checkerboard corners as reference world points of known coordinates which are localized in several images to establish pixel correspondences. In the projector case, we will project a known pattern onto a checkerboard and to record a set of images for each checkerboard pose. The projected pattern is later decoded from the camera images and used to convert from camera coordinates to projector pixel locations. This way, checkerboard corners are identified in the camera images and, with the help of the projected pattern, their locations in projector coordinates are inferred. Finally, projector-checkerboard correspondences are used to calibrate the projector parameters as it is done for cameras. This calibration method is described with detail in [MT12] and implemented as an opensource calibration and scanning tool[2]. We will use this software for projector and camera calibration when working with structured light scanners in Chapter 5. A step-by-step guide of calibration process is given below in Section 3.2.2.

3.2.1 Projector Selection and Interfaces

Almost any digital projector can be used in your 3D scanning projects, since the operating system will simply treat it as an additional display. However, we recommend at least a VGA projector, capable of displaying a 640×480 image. For building a structured lighting system select a camera with equal (or higher) resolution than the projector. Otherwise, the recovered model will be limited to the camera resolution. Additionally, those with DVI or HDMI interfaces are preferred for their relative lack of analogue to digital conversion artifacts.

The technologies used in consumer projectors have matured rapidly over the last decade. Early projectors used an LCD-based spatial light modulator and a metal halide lamp, whereas recent models incorporate a digital micromirror device (DMD) and LED lighting. Commercial offerings vary greatly, spanning large units for conference venues to embedded projectors for mobile phones. A variety of technical specifications must be considered when choosing the "best" projector for your 3D scanning projects. Variations in throw distance (i.e., where focused images can be formed), projector artifacts (i.e., pixelization and distortion), and cost are key factors.

Digital projectors have a tiered pricing model, with brighter projectors costing significantly

[2] http://mesh.brown.edu/scanning/software.html

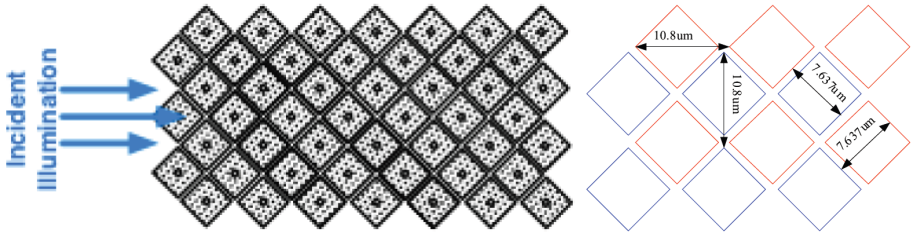

Figure 3.6: TI DLP .45in Pico Projectors diamond pixel configuration.

more than dimmer ones. At the time of writing, a portable projector with output resolution of 1280×800 and 100–500 lumens of brightness can be purchased for around $300–$500 USD. Examples are the Optoma and Dell Pico projectors shown in Figure 3.5 commonly used by students because of their convenient small size and high contrast.

When considering projectors it is important to distinguish between their "native" and "output" resolutions. Native resolution refers to the number of pixels in the projection device (i.e. number of micromirrors in DLPs arrays), whereas, the output resolution is the screen size reported to the operating system. Ideally, we want both to be the same so that images sent by the operating are displayed by the projector at the same resolution. However, many portable projectors use Texas Instruments DLP Pico DMDs where projector pixels are rotated 45° as shown in Figure 3.6. In this configuration the pixel density in the horizontal and vertical directions are different and images generated by the computer are resampled to match the DMD elements. We have used pico projectors in structured-light scanners successfully but the native resolution has to be considered to decide the maximum resolution of the projected patterns.

While your system will treat the projector as a second display, your development environment may or may not easily support fullscreen display. For instance, MATLAB does not natively support fullscreen display (i.e., without window borders or menus). One solution is to use Java display functions integrated in MATLAB. Code for this approach is available online[3]. Unfortunately, we found that this approach only works for the primary display. Another common approach is to split image acquisition and data processing in two separate programs and use standard software (i.e. as provided by camera manufacturers) to capture and save images, and to program your scanning tool to read images from a permanent storage. This approach is used by the Camera Calibration Toolbox [Bou]. Finally, for users working outside of MATLAB, we recommend controlling projectors through OpenGL.

3.2.2 Calibration Software and Procedure

Projector calibration has received increasing attention, in part driven by the emergence of low-cost digital projectors. As mentioned at several points, a projector is simply the "inverse" of a camera, wherein points on an image plane are mapped to outgoing light rays passing through the center of projection. As in Section 3.1.2, a lens distortion model can augment the basic general pinhole model presented in Chapter 2. In this section we will use the Projector-Camera Calibration software [MT] to calibrate both projector and camera, intrinsic and extrinsic parameters, including radial distortion coefficients. This software is built for Windows, Linux, and Mac OS X, and source code is available too.

Begin by downloading the software [MT] for your platform and setting up your projector and

[3] http://www.mathworks.com/matlabcentral/fileexchange/11112

Figure 3.7: Sample setup of a structured light scanner. A projector and camera are placed at similar height with a horizontal translation in stereo configuration. In this particular case, the camera is much forward than the projector to compensate between their different field of view.

camera in the scanning position. Once calibrated, projector and camera have to remain at fix positions, and their lens settings unchanged (e.g. focus, zoom) for the calibration to remain valid. The general recommendation is to place them with some horizontal displacement, too much displacement will provide little overlap between projector and camera images, too few displacement will produce a lot of uncertainty for triangulation, try to find some intermediate position, see Figure 3.7 as example. A checkerboard pattern is required for calibration.

Run the software and click the "Capture..." button to open a preview window, Figure 3.8. Select your projector screen and your camera using the combo boxes, then check "Preview" to activate the projector. Click "Prev" and "Next" buttons to navigate the projected pattern sequence as desired. Use the camera live view to make sure camera and projector view points are correct. Note that only cameras supported by OpenCV will be recognized by the software; if your camera happens to not be in this group, you can still use the tool for calibration but you will have to project and capture the images with an external software, and use the tool only for calibration. Refer to the software website for more details.

Place the calibration checkerboard in the scene in such a way that all its cells are visible in the camera and illuminated by the projector. Uncheck "Preview" and press "Capture". The software will project and capture a sequence of images. The checkerboard has to remain static at this time. The image output folder can be changed prior beginning, but it must not be changed after the first capture. Repeat the capture procedure several times to collect sequences with the checkerboard at

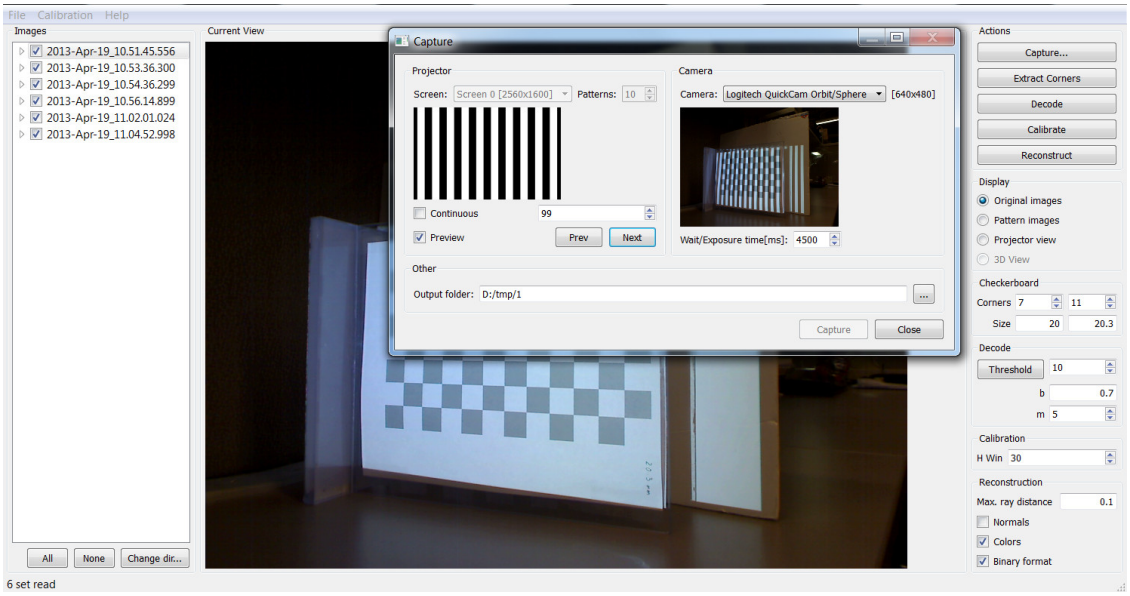

Figure 3.8: Projector-Camera Calibration software main screen and capture window.

different positions and orientations. Close the capture window to return to the main screen.

The main screen will display a list with the different sequences captured, which can be browsed to see any of the images. If images were captured with an external tool, or with this tool but at a different time, you can select their location by clicking "Change dir..". Count the internal number of corners of your checkerboard and fill the boxes labeled as "Corners", also measure them in millimeters, or your unit of choice, and enter their dimensions in the "Size" boxes. Now you are ready for calibration, click "Calibrate". The program will automatically detect the checkerboard corners, decode the projected sequences, and run the calibration. The final result will be displayed as text and saved to a file. The main screen contains other parameters and buttons that can be used to debug errors or to change the default decoding options, they will not be covered here but feel free to read the documentation and modify them to improve your results.

Chapter 4

The Laser Slit 3D Scanner

In this chapter we describe how to build the "classic" desktop Laser Slit 3D Scanner consisting of a single digital camera, a laser line projector, and a manual or motorized turntable. Specifically, we will describe how to setup the scanner using inexpensive elements, and we will describe its operating principle and the mathematics that allow to compute the 3D shape of an object being scanned.

4.1 Description

The Laser Slit 3D Scanner is an "active line scanner", meaning that it uses active illumination—the laser line projected onto a scene—and that it recovers a single line of points from each captured frame. Active illumination permits to scan objects more or less independently of their surface color or texture, which is an important advantage over passive methods which have difficulty in recovering constant color regions. On the other hand, a single line is captured at each time and it is necessary to move either the scanner or the object to acquire additional points and incrementally build a 3D model. In our case, we decided to put the target object onto an inexpensive turntable which is rotated manually in order to create a 360° model. Some users may prefer to use a computerized turntable controlled by a stepper motor for more automation or may want to do other variations to the suggested setup. The mathematics and methods discussed here will be applicable with little or no modification to many of these variations.

The scanner is setup as shown in Figure 4.1. The camera is fixed on a side, elevated from the turntable plane, and looking down to the turntable center. The optimal orientation and distance depends on the camera field-of-view and the size of scanning volume. The general guideline is that most of the turntable surface must be visible when there is no object on it, and the bottom and top of the object being scanned must be visible too when sitting on the turntable. It is not recommended to put the camera farther than required because the image regions looking at neither the turntable nor the target object will not be used by the scanner. The Laser Line Generator must be placed on a side of the camera and with similar orientation, it is recommended that it passes through the turntable center point and be orthogonal to the turntable plane. Figure 4.2 shows the materials we have used in our setup: a 650nm AixiZ 38° Line Generator, a Logitech HD Pro Webcam C920, and a manually controlled turntable.

We will set the world coordinate system at the turntable center of rotation, with the xy-plane on the turntable and the z-axis pointing up, see Figure 4.1. Prior to scanning, we need to calibrate the camera intrinsic parameters and the location of both the camera and light plane generated by the laser in respect to the world coordinate system. The turntable center of rotation must

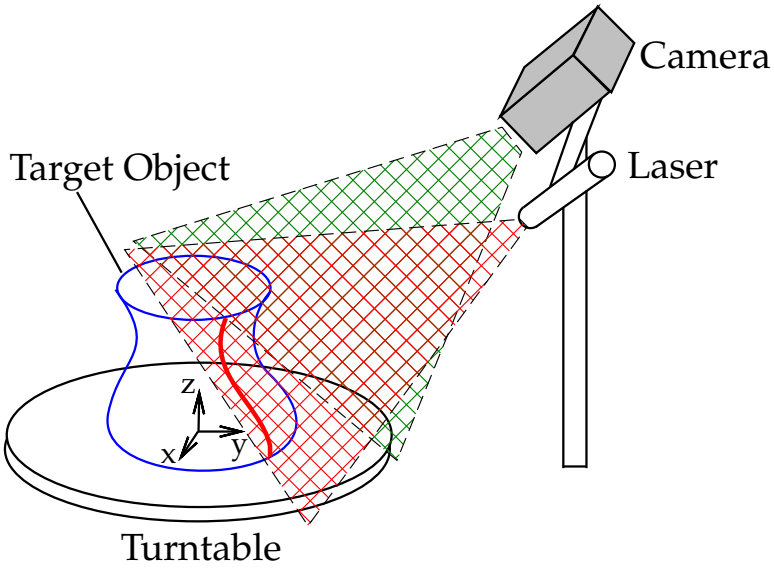

Figure 4.1: Laser Slit 3D Scanner setup

Figure 4.2: Materials: (Left) 650nm AixiZ 38° Line Generator. (Center) Logitech HD Pro Webcam C920. (Right) Manual turntable.

be calibrated too. At scanning time, the light plane generated by the laser is invisible in the air but we can see some of its points when the light hits a surface, they will have the color of the projected light (red in our case). These points can be detected in an image captured by the camera and its 3D location is found as the intersection of a ray beginning at the camera center, passing through the corresponding image pixel, and the plane of light (known), Figure 4.3. The location of the points recovered from each image must be rotated through the z-axis to undo the current turntable rotation angle.

4.2 Turntable calibration

A computer controlled turntable will provide us with the current rotation angle that corresponds to the stepper motor current rotation. Sometimes, as in the case of a manual turntable, that information is not available and the rotation must be computed from the current image. We will do so with the help of a CALTag checkerboard [AHH10] pasted flat on the turntable surface. The CALTag checkerboard assigns a unique code to each checkerboard cell which is used to identify the visible cells in an image even when a region of the checkerboard is occluded. We need this

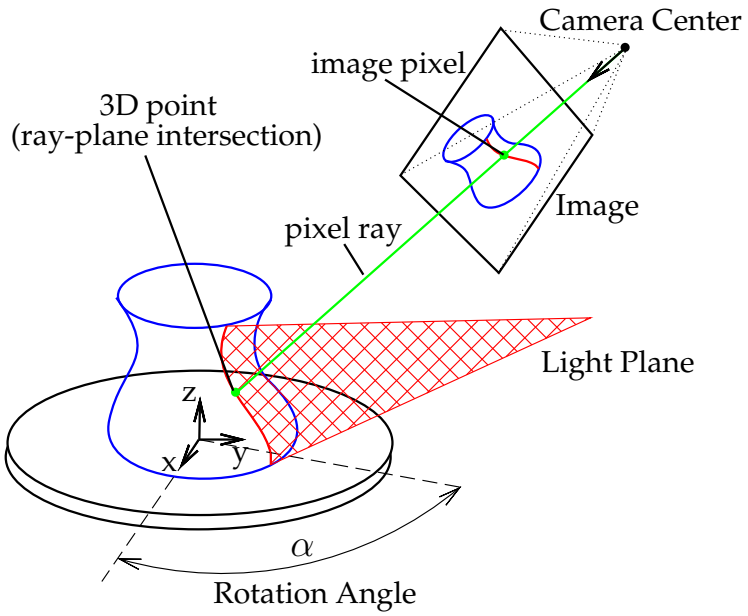

Figure 4.3: Laser Slit 3D Scanner setup

property because the target object sitting on top the turntable will occlude a large region of the CALTag. The corners of the visible checkerboard cells is a set of points rotating together with the turntable and will allow us to compute a rotation angle for each captured image.

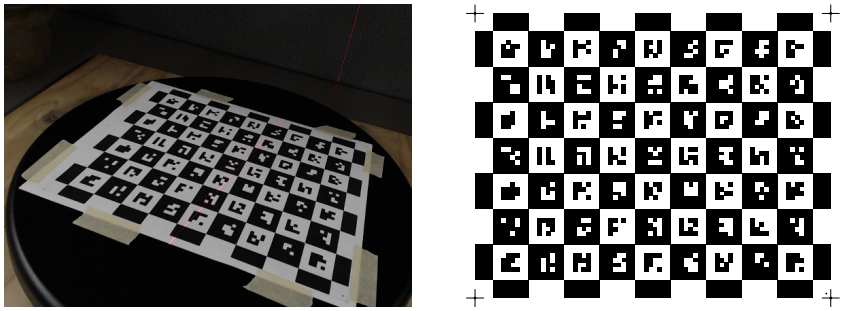

Figure 4.4: (Left) A CALTag checkerboard pasted on the turntable surface helps to recover the current rotation angle. (Right) Sample CALTag pattern.

At this point we assume the camera is calibrated and a set of images of the turntable at different rotations was captured. In addition, a set of 3D points on the turntable plane was identified in each image. Points coordinates are in reference to a known coordinate system chosen by the user. We will show how to find the unknown center of rotation and the rotation angle of the turntable for each image. In the current example, we align the coordinate system with the checkerboard and we identify the checkerboard and turntable planes with the plane $z = 0$.

4.2.1 Camera extrinsics

The first step is to find the pose of the camera for each image in reference to the known coordinate system. At this point we will compute a rotation matrix R and a translation vector T for each image independently of the others, such that a point p in the reference system projects to a pixel u, that is

$$\lambda u = K(Rp + T) \tag{4.1}$$

$$R = \begin{bmatrix} r_{11} & r_{12} & r_{13} \\ r_{21} & r_{22} & r_{23} \\ r_{31} & r_{32} & r_{33} \end{bmatrix},\ T = \begin{bmatrix} T_x \\ T_y \\ T_z \end{bmatrix} \tag{4.2}$$

where u, p, and K are known. Point $p = [p_x, p_y, 0]^T$ is in the checkerboard plane and $u = [u_x, u_y, 1]^T$ is expressed in homogenous coordinates. We define $\tilde{u} = K^{-1}u$ and rewrite Equation 4.1 as follows

$$[0,0,0]^T = \tilde{u} \times (\lambda\tilde{u}) = \tilde{u} \times (Rp + T) \tag{4.3}$$

$$\tilde{u} \times \begin{bmatrix} r_{11}p_x + r_{12}p_y + T_x \\ r_{21}p_x + r_{22}p_y + T_y \\ r_{31}p_x + r_{32}p_y + T_z \end{bmatrix} = \begin{bmatrix} 0 \\ 0 \\ 0 \end{bmatrix} \tag{4.4}$$

$$\begin{bmatrix} -(r_{21}p_x + r_{22}p_y + T_y) & + & \tilde{u}_y(r_{31}p_x + r_{32}p_y + T_z) \\ (r_{11}p_x + r_{12}p_y + T_x) & - & \tilde{u}_x(r_{31}p_x + r_{32}p_y + T_z) \\ -\tilde{u}_y(r_{11}p_x + r_{12}p_y + T_x) & + & \tilde{u}_x(r_{21}p_x + r_{22}p_y + T_y) \end{bmatrix} = \begin{bmatrix} 0 \\ 0 \\ 0 \end{bmatrix}. \tag{4.5}$$

Equation 4.5 provides 3 equations but only 2 of them are linearly independent. We select the first two equations and we group the unknowns in a vector $X = [r_{11}, r_{21}, r_{31}, r_{12}, r_{22}, r_{32}, T_x, T_y, T_z]^T$

$$\begin{bmatrix} 0 & -p_x & +\tilde{u}_y p_x & 0 & -p_y & +\tilde{u}_y p_y & 0 & -1 & +\tilde{u}_y \\ p_x & 0 & -\tilde{u}_x p_x & p_y & 0 & -\tilde{u}_x p_y & 1 & 0 & -\tilde{u}_x \end{bmatrix} X = \begin{bmatrix} 0 \\ 0 \end{bmatrix}. \tag{4.6}$$

Until now we have considered a single point p; in general, we will have a set of points $\{p_i | i : 1 \dots n\}$ for each image. Note that the number n of points visible will change from image to image. We use all the points to build a single system of the form $AX = 0$ where $A \in \mathbb{R}^{2n \times 9}$ contains 2 rows as in Equation 4.6 for each point p_i stacked together, and we solve

$$\hat{X} = arg\min_X ||AX||, \quad \text{s.t. } ||X|| = 1 \tag{4.7}$$

We constrain the norm of X in order to get a non-trivial solution. Vector X has 8 degrees of freedom, thus, matrix A must be rank 8 so that a unique solution exists. Therefore, we need at least 4 non-collinear points in order to get a meaningful result. After solving for $\hat{X}$ we need to rebuild R as a rotation matrix.

$$\hat{r_1} = [r_{11}, r_{21}, r_{31}]^T,\ \hat{r_2} = [r_{21}, r_{22}, r_{23}]^T,\ \hat{T} = [T_x, T_y, T_z]^T, s = \frac{2}{||\hat{r_1}|| + ||\hat{r_2}||} \tag{4.8}$$

$$r_1 = s\,\hat{r_1},\ r_3 = r_1 \times s\,\hat{r_2},\ r_2 = r_3 \times r_1 \tag{4.9}$$

$$R = \begin{bmatrix} r_1 & r_2 & r_3 \end{bmatrix},\ T = s\,\hat{T} \tag{4.10}$$

Figure 4.5 shows the supplied software running the camera extrinsics computation as described here.

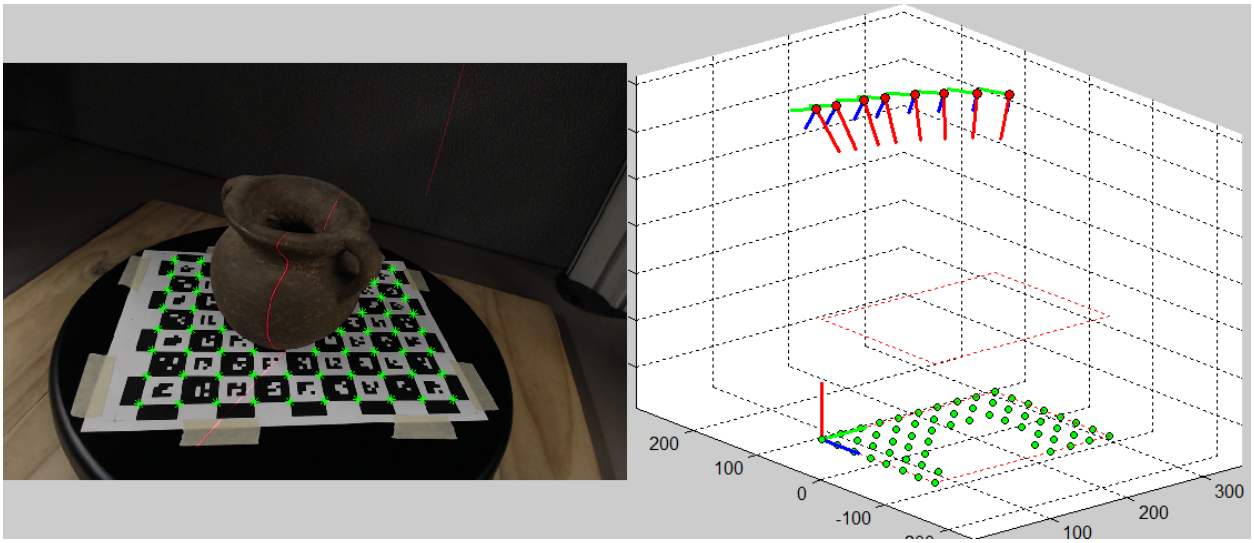

Figure 4.5: Screenshot of the supplied software running camera extrinsics computation. (Left) Image being processed: identified CALTag corners displayed in green. (Right) 3D view: CALTag corners shown in green below, cameras displayed above with their z-axis on red, the reference coordinate system was set at the origin of the checkerboard.

4.2.2 Center of rotation and rotation angle

In the previous section we showed how to estimate R_k and T_k for each of the N cameras independently. Now, we will use the fact that the turntable rotates in a plane and has a single degree of freedom to improve the computed camera poses. We begin finding the center of rotation $q = [q_x, q_y, 0]^T$ in the turntable plane which must satisfy the projection equations as any other point

$$\lambda_k \tilde{u}_k = R_k q + T_k \tag{4.11}$$

By definition of rotation center its position remains unchanged before and after the rotation, this observation allow us to define $Q \equiv \lambda_k \tilde{u}_k, \ \forall k$, and write

$$R_k q + T_k = Q \tag{4.12}$$

$$\begin{bmatrix} R_1 & -I \\ R_2 & -I \\ \vdots & \vdots \\ R_N & -I \end{bmatrix} \begin{bmatrix} q \\ Q \end{bmatrix} = \begin{bmatrix} -T_1 \\ -T_2 \\ \vdots \\ -T_N \end{bmatrix} \Rightarrow \ AX = b \tag{4.13}$$

$$\hat{X} = arg \min_X ||AX - b|| \tag{4.14}$$

In order to fix $q_z = 0$, we skip the third column in the rotation matrices reducing A to 5 columns and changing $X = [q_x, q_y, Q_x, Q_y, Q_z]^T$.

Let be α_i the rotation angle of the turntable in image i, then for every $1 \leq k < j \leq N$, we should have

$$R_k^T R_j = \begin{bmatrix} \cos(\alpha_j - \alpha_k) & -\sin(\alpha_j - \alpha_k) & 0 \\ \sin(\alpha_j - \alpha_k) & \cos(\alpha_j - \alpha_k) & 0 \\ 0 & 0 & 1 \end{bmatrix} \tag{4.15}$$

The turntable position in the first image is designated as the origin: $\alpha_1 = 0$. We get an approximate value for each other α_k by reading the values $\cos\alpha_k$ and $\sin\alpha_k$ from $R_1^T R_k$ and setting

$$\alpha_k = \tan^{-1}\left(\frac{\sin\alpha_k}{\cos\alpha_k}\right) \tag{4.16}$$

Figure 4.6 shows the center of rotation obtained with this method drawn on top of an input image and its corresponding 3D view.

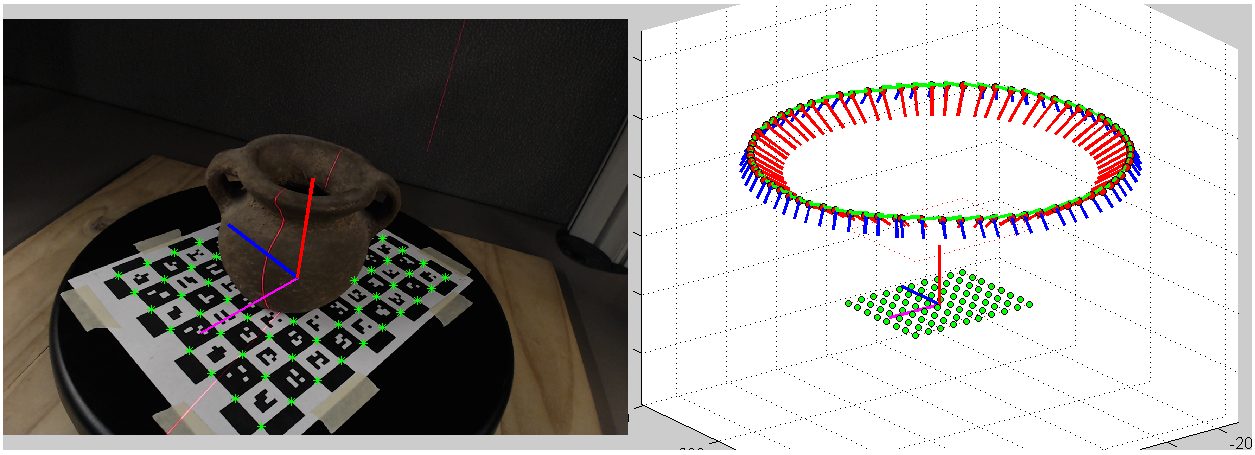

Figure 4.6: Center of rotation. (Left) Camera image: center of rotation drawn on top. (Right) 3D view: world coordinate system at the center of the rotation.

4.2.3 Global optimization

The final step in turntable calibration is to refine the values of all the parameters using a global optimization. The goal is to minimize the reprojection error of the detected points in the images

$$E(q_x, q_y, R_1, o_1, \alpha_2, \ldots, \alpha_N) = \sum_{k=1}^{N}\sum_{i\in J_k} ||u_k^i - \Pi(K R_1 R_{\alpha_k}(p_i - o_k))||^2 \tag{4.17}$$

where

$$R_{\alpha_k} = \begin{bmatrix} \cos(\alpha_k) & -\sin(\alpha_k) & 0 \\ \sin(\alpha_k) & \cos(\alpha_k) & 0 \\ 0 & 0 & 1 \end{bmatrix},\ o_k = R_{\alpha_k}^T(o_1 - q) + q,\ \ \forall k > 1, \tag{4.18}$$

and

$$\Pi(x, y, z) = (x/z, y/z) \tag{4.19}$$

J_k is the subset of checkerboard corners visible in image k, $\alpha_1 = 0$, and u_k^i is the pixel location corresponding to p_i in image k. We begin the optimization with the values q, R_1, $o_1 = -R_1^T T_1$, and α_k found in the previous sections which are close to the optimal solution.

4.3 Image Laser Detection

In this section we show how to detect the laser slit in the captured images. A common approach to detection is to compare an image where the laser is seen with a reference image captured while

the laser is off. That approach is appropriate for a scanner setup where the camera and the object remains static while the laser changes location. Detection is done by subtracting the intensity in the new image with the reference intensity and searching the pixels where a significance change is observed. This method works independently of the laser color, would work even when color images are not available, it is computationally efficient, and most importantly, it is tuned to the current scene and illumination, because a new reference image is captured for each new scanning. However, the method is not applicable if a reference image is not available, or as in the case of the turntable where we would need as many reference images as turntable positions.

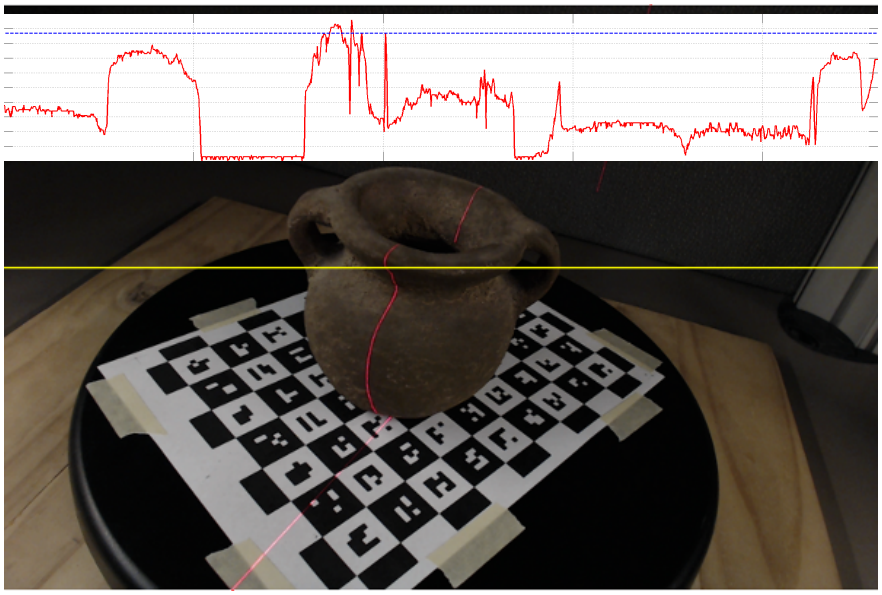

Figure 4.7: The plot shows the red channel intensity along the line in the image highlighted in yelow. The maximum value does not corresponds to the laser line.

In our scanner we will apply a laser detection algorithm that considers the laser color and it does work with a single image. In our case we used a red laser and we could expect to examine the image red channel and find a maximum at the laser location. This is not always true even if there are no other red points in the scene. For instance, Figure 4.7 shows a typical input image, without any red color visible besides the laser line, but the highlighted line contains many pixels with red intensity above the value at the laser location, indicated with a blue line in the plot. The reason is that red color is not the one with a high value in the red channel—white has high intensities in all channels. The property of red color is that it *only* has a high intensity in the red channel. Based on this observation we will perform the detection in a "channel difference image" defined as

$$I_{diff} = I_r - \frac{I_g + I_b}{2} \tag{4.20}$$

where I_r, I_g, and I_b are the image red, green, and blue channels respectively. Figure 4.8 shows I_{diff} for the sample image. Now, there is a clear peak at the laser location.

Our detection algorithm involves computing the channel difference image with Equation 4.20 and finding its maximum row by row. In general, we hope to find a single or no laser slit point in each row because we have oriented the laser line generator vertically. However, in rare occasions may appear more than one laser slit per line due to object discontinuities. For simplicity, we will consider only the one with maximum intensity.

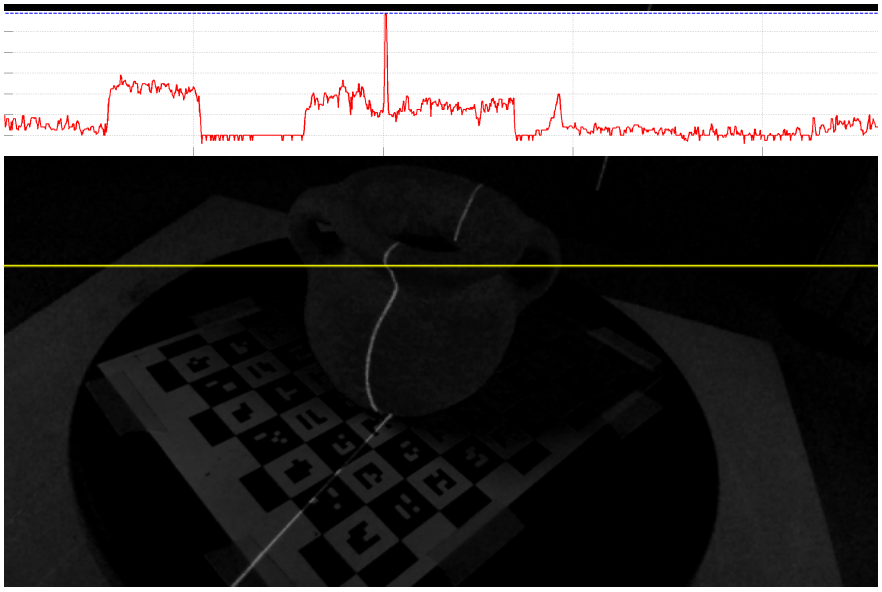

Figure 4.8: Channel difference. The image and plot show a clear peak at the laser line location.

Laser line generators made with a cylinder lens produce a Gaussian light distribution. In practice, cheap lenses have a profile not so well defined and the observed maximum will vary randomly in a range close to the line center, Figure 4.9. In order to compensate and make the estimation more stable from row to row, it is recommended to apply Gaussian smoothing in the horizontal direction prior to searching the maximum.

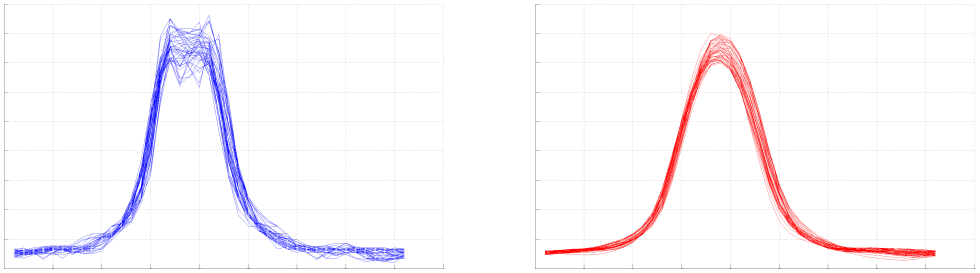

Figure 4.9: Laser line intensity plot of several image rows of similar color: (Left) there is no clear maximum at the peak center, (Right) the maximum is well localized after smoothing.

Figure 4.10 shows the result of the single image laser stripe detection described to the sample image.

4.4 Background detection

It is desirable to detect and exclude the background from the scanning process. Doing so saves computation on unwanted image regions, reduces detection errors, and produces a 3D model only with the object of interest. A pixel imaging a point on the turntable or the object sitting on top of it will be considered as foreground, all the other pixels are considered background. The set of foreground and background pixels are disjoint and the union of them contains the whole image.

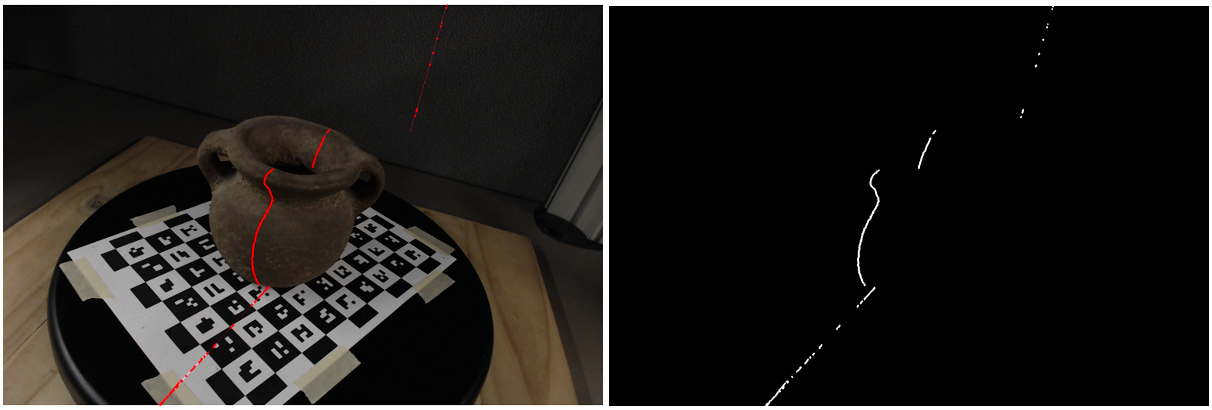

Figure 4.10: Laser detection result: (Left) detected points overlapped in red to input image, (Right) detection result mask.

Additionally, a pixel location could be background in one image and foreground on a different one. Our goal is to compute the intersection of all images background pixels, that is, identify the pixel locations that are never foreground and we would like exclude from further processing.

By definition, a pixel location that is always background will have constant intensity. In reality, a background pixel will have little intensity variations due to the image sensor noise and small illumination changes. We can check this property by calculating the intensity variance of each pixel in the whole image set and label as background those with small variances.

Figure 4.11 (Left and Middle) verifies the constant property of background pixels visually. The background in the mean image is seen sharp, whereas, foreground pixels are blurred due to their changing intensities. Background pixels are close to zero (black) in the variance image. The detection result is displayed as a binary mask in Figure 4.11 (Right), foreground is shown in white.

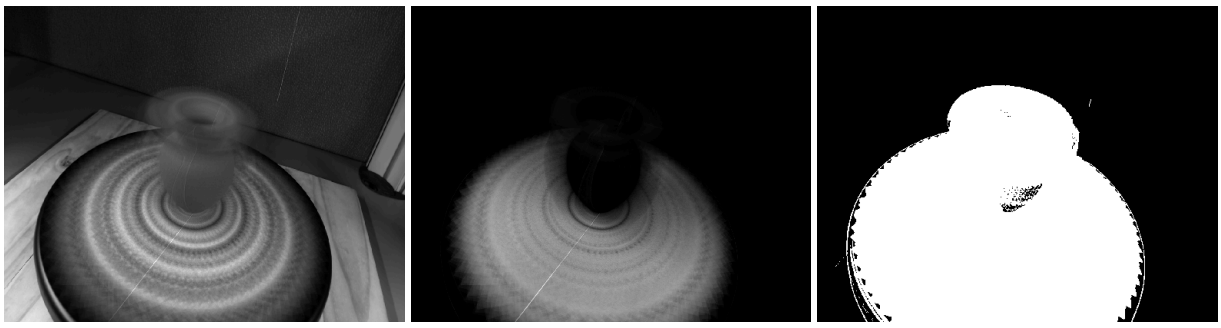

Figure 4.11: Background detection: (Left) mean intensity image, (Middle) variance intensity image, (Right) background mask result.

4.5 Plane of light calibration

We need to calibrate the location of the plane of light generated by the laser. The calibration consists in identifying some points we know belong to the plane and finding the best plane, in the least squares sense, that matches them. The projection of the laser line onto the turntable provides us with a set of such points, however, they are all in a straight line and define a pencil of planes

rather a single one. An easy way to find additional points is to place a checkerboard plane onto the turntable and capture images at several rotations, Figure 4.12.

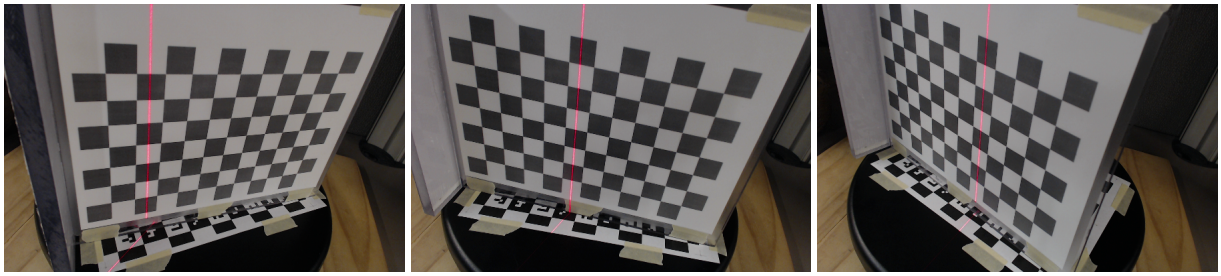

Figure 4.12: Light plane calibration: an extra plane is placed onto the turntable and is rotated to provide a set of non-collinear points.

The orientation of the camera with respect to the checkerboard plane is calculated with the method from Section 4.2.1. The laser pixels are identified with the detection algorithm and they are triangulated using ray-plane intersection providing a set of 3D points on the checkerboard plane. We can choose to triangulate the laser points on the turntable plane too, which makes possible to calibrate with a single image. It is recommendable to capture additional images to have more samples of the light plane for a better calibration. In special, we would like samples at different depths in the scanning volume. Checkerboard images captured for the camera intrinsic calibration can be reused to calibrate the plane of light, this way no extra images are required. This idea is illustrated in Figure 4.13.

4.6 3D model reconstruction

At this point the system is fully calibrated: camera internal parameters, camera pose, world coordinate system, turntable rotation angle in each image, and the plane of light are all known. The last step is to identify the laser slits corresponding to the target object, triangulate them by ray-plane intersection with the light plane, and place the result in the world coordinate system by undoing the turntable rotation at each image. To generate only points in the model only foreground pixels are triangulated, and only the 3D points within the scanning volume are added to the model. The scanning volume is easily defined as the rectangular region of the turntable checkerboard and extending vertically in the direction of the z-axis by a user given height. Figure 4.14 shows the result output following the methods from this chapter and without any additional post-processing.

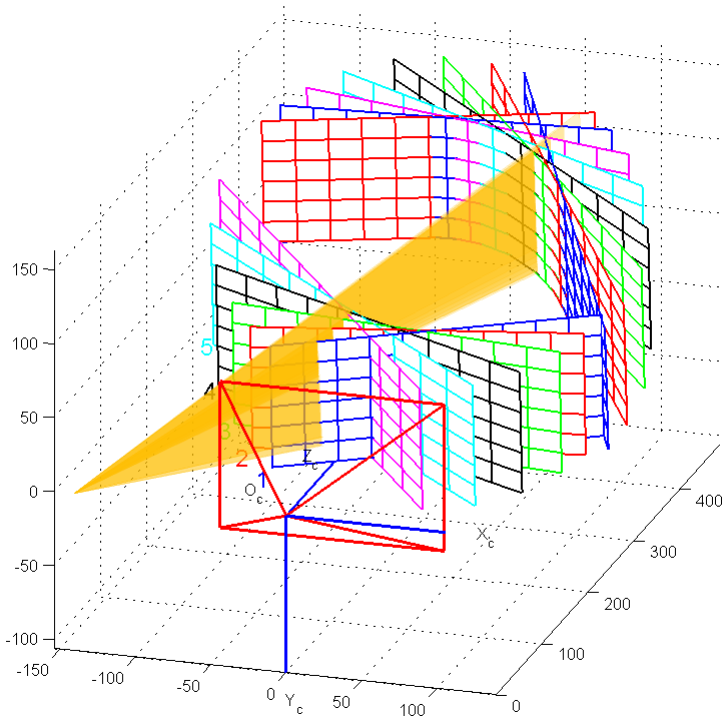

Figure 4.13: Light plane calibration result. A checkerdboard plane was placed on the turntable and images at several rotations were captured. Images are used first for camera calibration, and later for calibration of the light plane (shown in orange).

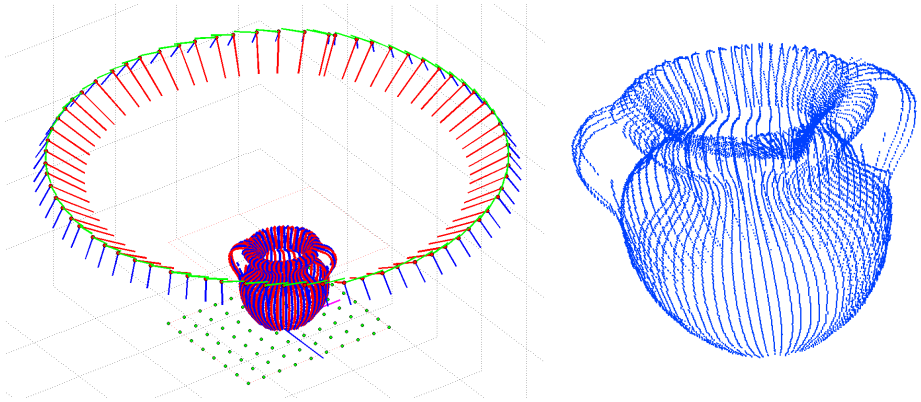

Figure 4.14: Laser Slit 3D Scanner result: (Left) 3D model in the sample software, (Right) 3D model output.

Chapter 5

Structured Lighting

In this chapter we describe how to build a structured light scanner using one or more digital cameras and a single projector. While the Laser Slit 3D Scanner implemented in the previous chapter is widely used, it needs hundreds of images to build a complete model with acceptable detail. It could be argued that the scanning process is inefficient, in the sense that only a very small set of pixels illuminated by the laser contribute to the scan in each image, and the rest are mostly ignored. On the contrary, a Structured Light Scanner replaces the projected laser line with a data projector capable of displaying 2-dimensional patterns covering a much larger object region, and generating a 3D model containing all the points being simultaneously illuminated by the projector and visible from the cameras. More information is extracted from each image, thus, reducing the number of images required and the total scanning time. A turntable is still useful, but only a few rotations will be required to build a full model.

The structured light scanner builds on top of the theory and algorithms developed in the previous chapters. Reconstruction is now accomplished using ray-ray triangulation between projector and camera pixels. The key concept here is that correspondences are established by decoding certain structured light sequences. The methods described below are already implemented in the Projector-Camera Calibration software introduced in Chapter 3. Here we will expand on how projector columns and rows are coded in the patterns and later decoded from the camera images.

5.1 Structured Light Scanner

Structured light scanners became highly popular in the recent years, mainly because of the low cost and wide availability of quality data projectors and cameras. The concept of structured light refers to the idea of the scene being illuminated by specially designed patterns. A quick review of the literature will reveal that many different patterns have been proposed using different coding strategies. Salvi et al. [SFPL10] give several pattern classifications depending on whether they make use of color, the number of images required, the type of encoding, and whether they encode discrete or continuous quantities, a few examples are shown in Figure 5.1. We will focus only on discrete binary patterns and a minor variant known as Gray code, both are shown in Figures 5.3 and 5.4.

5.1.1 Scanner Hardware

Our scanner is built with a single camera and a single data projector. This choice replicates passive stereo scanners which observe a scene with a pair of cameras and build a 3D model by triangulating points visible in both of them. Identifying the exact position where points from the first view

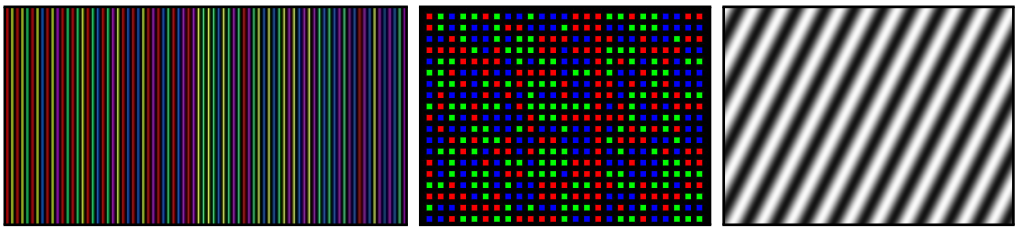

(a) De Bruijn color stripes (b) Color M–Array (c) Phase shifting

Figure 5.1: Patterns with different coding strategies.

appear in the second view is a difficult task in general, known as "establishing pixel correspondences". Here, we replace one camera by a projector to simplify this task. As with other systems, several cameras and projectors could be added to extend the scanned area, or to provide more accurate measurements, but we will not discuss those variants here, however, once understood the concepts from this chapter, it should be more or less straightforward to generalized them to other configurations.

We will use the Logitech C920 Webcam and an Optoma ML550 projector setup as in Figure 5.2. The target object may be placed on a turntable and several scans can be aligned to build a 360° model by calibrating the turntable as in Section 4.2. It is advisable to mount the camera and projector in a tripod because they must remain fixed at all times.

Figure 5.2: Structured light scanner sample setup: Optoma ML550 projector, Logitech C920 Webcam, target object on a turntable, and computer.

5.1.2 Structured Light Sequences

The primary benefit of introducing the projector is to eliminate the mechanical motion required in the Laser Slit 3D Scanner. Assuming minimal lens distortion, the projector can be used to display

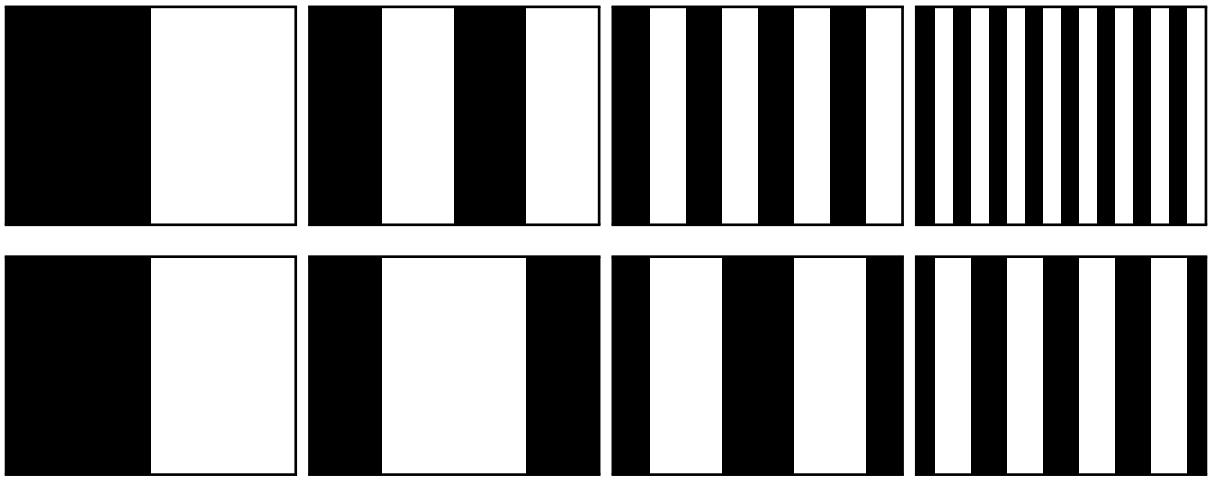

Figure 5.3: Structured light illumination sequences. (Top row, left to right) The first four bit planes of a binary encoding of the projector columns, ordered from most to least significant bit. (Bottom row, left to right) The first four bit planes of a Gray code sequence encoding the projector columns.

a single column (or row) of white pixels translating against a black background; thus, as many images as columns (or rows) in the projector would be required in order to assign the correspondences, in our implementation, between camera pixels and projector columns (or rows). After establishing the correspondences and calibrating the system, a 3D point cloud is reconstructed using familiar ray-plane triangulation. However, a simple strategy like this does not fully exploit the projector. Since we are free to project arbitrary 24-bit color images, one would expect there to exist a sequence of coded patterns, besides a simple translation of a single stripe, that allow the projector-camera correspondences to be assigned in relatively few frames. In general, the identity of each plane can be encoded spatially (i.e., within a single frame) or temporally (i.e., across multiple frames), or with a combination of both spatial and temporal encodings. There are benefits and drawbacks to each strategy. For instance, purely spatial encodings allow a single static pattern to be used for reconstruction, enabling dynamic scenes to be captured. Alternatively, purely temporal encodings are more likely to benefit from redundancy, reducing reconstruction artifacts.

In this chapter we will focus on purely temporal encodings. While such patterns are not well-suited to scanning dynamic scenes, they have the benefit of being easy to decode and are robust to surface texture variation, producing accurate reconstructions for static objects (with the normal prohibition of transparent or other problematic materials). A simple binary structured light sequence was first proposed by Posdamer and Altschuler [PA82] in 1981. As shown in Figure 5.3, the binary encoding consists of a sequence of binary images in which each frame is a single bit plane of the binary representation of the integer indices for the projector columns (or rows). For example, column 546 in our prototype has a binary representation of 1000100010 (ordered from the most to the least significant bit). Similarly, column 546 of the binary structured light sequence has an identical bit sequence, with each frame displaying the next bit.

Considering the projector-camera arrangement as a communication system, then a key question immediately arises; what binary sequence is most robust to the known properties of the channel noise process? At a basic level, we are concerned with assigning an accurate projector column/row to camera pixel correspondence, otherwise triangulation artifacts will lead to large reconstruction errors. Gray codes were first proposed as one alternative to the simple binary encoding by Inokuchi et al. [ISM84] in 1984. The *reflected binary code* was introduced by Frank Gray

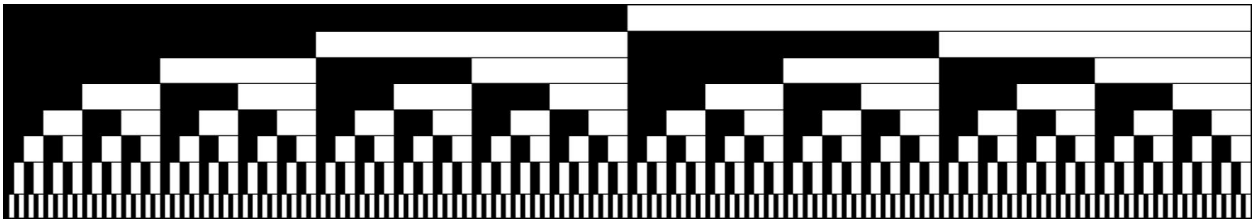

(a) binary structured light sequence

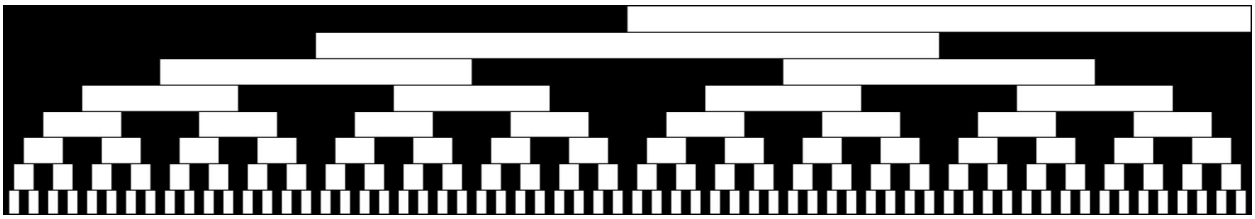

(b) Gray code structured light sequence

Figure 5.4: Comparison of binary (top) and Gray code (bottom) structured light sequences. Each image represents the sequence of bit planes displayed during data acquisition. Image rows correspond to the bit planes encoding the projector columns, assuming a projector resolution of 1024×768, ordered from most to least significant bit (from top to bottom).

BIN2GRAY(B)
1 $n \leftarrow length[B]$
2 $G[1] \leftarrow B[1]$
3 **for** $i \leftarrow 2$ **to** n
4 **do** $G[i] \leftarrow B[i-1]$ xor $B[i]$
5 **return** G

GRAY2BIN(G)
1 $n \leftarrow length[G]$
2 $B[1] \leftarrow G[1]$
3 **for** $i \leftarrow 2$ **to** n
4 **do** $B[i] \leftarrow B[i-1]$ xor $G[i]$
5 **return** B

Table 5.1: Pseudocode for converting between binary and Gray codes. (Left) BIN2GRAY accepts an n-bit Boolean array, encoding a decimal integer, and returns the Gray code G. (Right) Conversion from a Gray to a binary sequence is accomplished using GRAY2BIN.

in 1947 [Wik]. As shown in Figure 5.4, the Gray code can be obtained by reflecting, in a specific manner, the individual bit-planes of the binary encoding. Pseudocode for converting between binary and Gray codes is provided in Table 5.1. For example, column 546 in our implementation has a Gray code representation of 1100110011, as given by BIN2GRAY. The key property of the Gray code is that two neighboring code words (e.g., neighboring columns in the projected sequence) only differ by one bit (i.e., adjacent codes have a Hamming distance of one). As a result, the Gray code structured light sequence tends to be more robust to decoding errors than a simple binary encoding and binary codes should no be used in general.

5.2 Image Processing

The algorithms used to decode the structured light sequences described in the previous section are relatively straightforward. For each camera, it must be determined whether a given pixel is directly illuminated by the projector in each displayed image. If it is illuminated in any given frame, then the corresponding code bit is set high, otherwise it is set low. The decimal integer

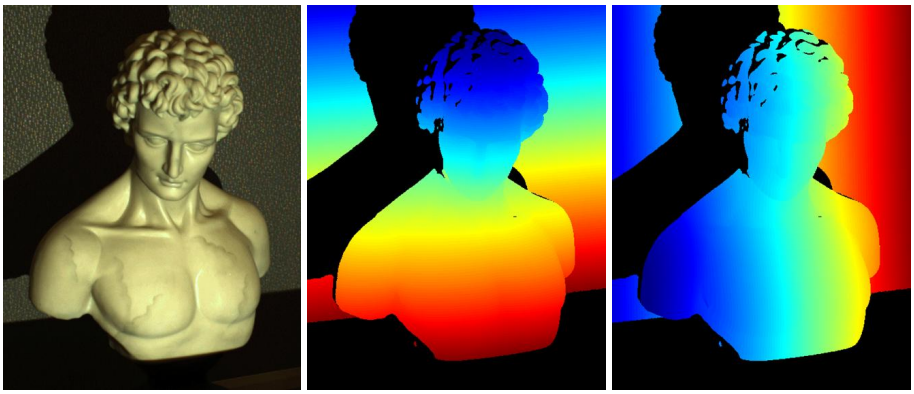

(a) all-white image (b) decoded row indices (c) decoded column indices

Figure 5.5: Decoding structured light illumination sequences. (a) Camera image captured while projecting an all white frame. Note the shadow cast on the background plane, prohibiting reconstruction in this region. (b) Typical decoding results for a Gray code structured light sequence, with projector row and camera pixel correspondences represented using a `jet` colormap in MATLAB. Points that cannot be assigned a correspondence with a high confidence are shown in black. (c) Similar decoding results for projector column correspondences.

index of the corresponding projector column (and/or row) can then be recovered by decoding the received bit sequences for each camera pixel. A user-selected intensity threshold is used to determine whether a given pixel is illuminated. For instance, $\lceil \log_2 w \rceil + 2$ images could be used to encode the projector columns, with the additional two images consisting of all-white and all-black frames. The average intensity of the all-white and all-black frames could be used to assign a per-pixel threshold; the individual bit planes of the projected sequence could then be decoded by comparing the received intensity to the threshold.

In practice, a single fixed threshold results in decoding artifacts. For instance, certain points on the surface may only receive indirect illumination scattered from directly-illuminated points. In certain circumstances the scattered light may cause a bit error, in which an unilluminated point appears illuminated due to scattered light. Depending on the specific structured light sequence, such bit errors may produce significant reconstruction errors in the 3D point cloud. One solution is to project each bit plane and its inverse. While $2\lceil \log_2 w \rceil$ frames are now required to encode the projector columns, the decoding process is less sensitive to scattered light, since a variable per-pixel threshold can be used. Specifically, a bit is determined to be high or low depending on whether a projected bit-plane or its inverse is brighter at a given pixel. Typical decoding results are shown in Figure 5.5.

The provided software [MT] uses a Gray code sequence and its inverse, for both columns and rows, plus the all-white and all-black images, but it implements a method called "Robust pixel classification" [XA07] to decide if a pixel was white, black, or it is set as "unknown" if cannot be decided. Robust pixel classification provides a set of rules designed to take into account that indirect illumination may cause some pixels to appear brighter than they should be. The rules require to separate each image into "global illumination" and "direct illumination" components. We call direct illumination the light which hits the scene "coming directly" from the projector, and global illumination any other light contributions including the ambient light. Implementing the robust classification is optional but we have found that the result improves without adding much decoding overhead.

As with any communication system, the design of structured light sequences must account for anticipated artifacts introduced by the communication channel. In a typical projector-camera system decoding artifacts are introduced from a wide variety of sources, including projector or camera defocus, scattering of light from the surface, and temporal variation in the scene (e.g., varying ambient illumination or a moving object). We have provided a variety of data sets for testing your decoding algorithms. In particular, the man sequence has been captured using both binary and Gray code structured light sequences. Furthermore, both codes have been applied when the projector is focused and defocused at the average depth of the sculpture. We encourage the reader to study the decoding artifacts produced under these non-ideal, yet commonly encountered, circumstances.

5.3 Calibration

The structured light scanner uses the triangulation principle to reconstruct the scanned model. In order to map pixel positions to world rays the system must be calibrated. In our case, we need to find the intrinsic parameters of the camera and projector, and the relative rotation and translation between them. If a turntable is used, the world coordinate system must be placed at its center of rotation as in the previous chapter, which has to be calibrated, and the rotation and translation from world coordinates to camera coordinates must be found. Without a turntable, the world coordinate system may be placed at the camera (or projector) center and with the same orientation. We will use the Projector-Camera Calibration software [MT] to calibrate everything but the turntable, which must be calibrated as in Section 4.2.

5.4 Reconstruction

The decoded set of camera and projector correspondences can be used to reconstruct a 3D point cloud. Several reconstruction schemes can be implemented using the sample sequences. The projector column correspondences can be used to reconstruct a point cloud using ray-plane triangulation. A second point cloud can be reconstructed using the projector row correspondences. Finally, the projector pixel to camera pixel correspondences can be used to reconstruct the point cloud using ray-ray triangulation (i.e., by finding the closest point to the optical rays defined by the projector and camera pixels). A simple per-point RGB color can be assigned by sampling the color of the all-white camera image for each 3D point. Reconstruction artifacts can be further reduced by comparing the reconstruction produced by each of these schemes. Typical results are shown in Figures 5.6–5.9.

The provided software implements ray-ray triangulation between camera and projector pixels, using the approximate intersection from Section 2.3.2. In order to remove errors, the minimum distance between rays is also computed and compared with a user-set threshold, a small distance is considered as intersection and a 3D point is created, otherwise the point is ignored. As usual, if the dimensions of the scanning volume is available, or can be roughly estimated, only points within the volume must be added to the model.

Figure 5.6: Reconstruction of the chiquita Gray code sequence.

Figure 5.7: Reconstruction of the schooner Gray code sequence.

Figure 5.8: Reconstruction of the urn Gray code sequence.

Figure 5.9: Reconstruction of the drummer Gray code sequence.

5.5 Sample software

The structured light scanner produces a colored 3D point cloud. Only points that are both imaged by a camera and illuminated by the projector can be reconstructed. As a result, a complete 3D model of an object would typically require merging multiple scans obtained by moving the scanning apparatus or object (e.g., by using a turntable). These issues are considered in Chapter 6.

We encourage the reader to implement their own solution so that measurements from multiple cameras, projectors, and 3D point clouds can be merged. As a reference the Projector-Camera Calibration software described Chapter 3 implements both the calibration and scanning using a structured light system.

Data acquisition for scanning is identical as how the calibration sequences were collected. A reconstruction for each individual sequence is performed by highlighting the sequence folder name in the list on the left part of the main screen and clicking "Reconstruct". Once the reconstruction is complete a file save dialog will open asking a pointcloud file name. At the time of writing, the software does not include a visualization of the result but the generated file can be opened using a standard 3D viewer (e.g. Meshlab [mes]). The software can reconstruct as many scans of an object as required but it will not merge them into a single model, each reconstruction will be stored as a separate pointcloud and must be merged using a separate software. Optionally, the surface normal at each point is estimated and added to the output creating an "oriented pointcloud" instead. Normals are useful to create more interesting visualizations and they are usually required by surface reconstruction tools.

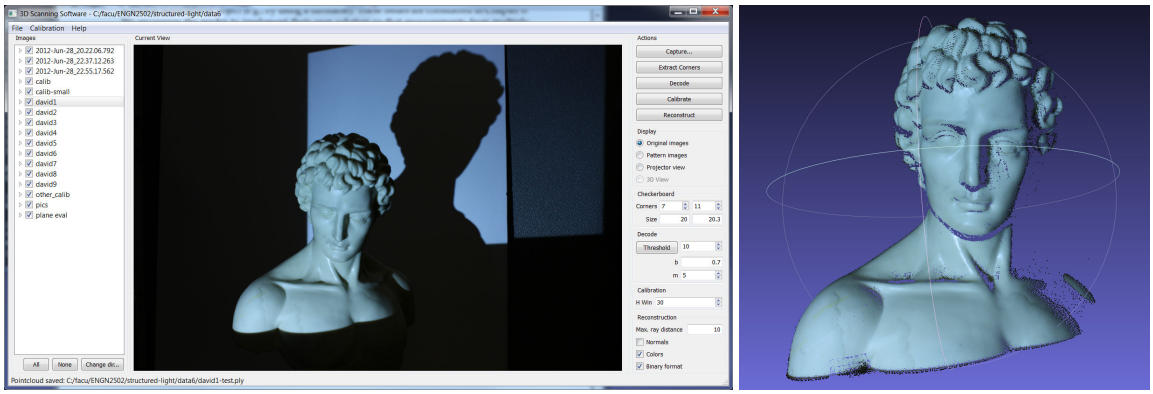

(a) Software main screen (b) 3D model result

Figure 5.10: Scanning example using the Projector-Camera Calibration software.

Chapter 6

Surfaces from Point Clouds

The objects scanned in the previous examples are solid, with a well-defined boundary surface separating the inside from the outside. Since computers have a finite amount of memory and operations need to be completed in a finite number of steps, algorithms can only be designed to manipulate surfaces described by a finite number of parameters. Perhaps the simplest surface representation with a finite number of parameters is produced by a finite sampling scheme, where a process systematically chooses a set of points lying on the surface.

The triangulation-based 3D scanners described in previous chapters produce such a finite sampling scheme. The so-called *point cloud*, a dense collection of surface samples, has become a popular representation in computer graphics. However, since point clouds do not constitute surfaces, they cannot be used to determine which 3D points are inside or outside of the solid object. For many applications, being able to make such a determination is critical. For example, without closed bounded surfaces, volumes cannot be measured. Therefore, it is important to construct so-called *watertight* surfaces from point clouds. In this chapter we consider these issues.

6.1 Representation and Visualization of Point Clouds

In addition to the 3D point locations, the 3D scanning methods described in previous chapters are often able to estimate a color per point, as well as a surface normal vector. Some methods are able to measure both color and surface normal, and some are able to estimate other parameters which can be used to describe more complex material properties used to generate complex renderings. In all these cases the data structure used to represent a point cloud in memory is a simple array. A minimum of three values per point are needed to represent the point locations. Colors may require one to three more values per point, and normals vectors three additional values per point. Other properties may require more values, but in general it is the same number of parameters per point that need to be stored. If M is the number of parameters per point and N is the number of points, then point cloud can be represented in memory using an array of length NM.

6.1.1 File Formats

Storing and retrieving arrays from files is relatively simple, and storing the raw data either in ASCII format or in binary format is a valid solution to the problem. However, these solutions may be incompatible with many software packages. We want to mention two standards which have support for storing point clouds with some auxiliary attributes.

Storing Point Clouds as VRML Files

The Virtual Reality Modeling Language (VRML) is an ISO standard published in 1997. A VRML file describes a scene graph comprising a variety of nodes. Among geometry nodes, `PointSet` and `IndexedFaceSet` are used to store point clouds. The `PointSet` node was designed to store point clouds, but in addition to the 3D coordinates of each point, only colors can be stored. No other attributes can be stored in this node. In particular, normal vectors cannot be recorded. This is a significant limitation, since normal vectors are important both for rendering point clouds and for reconstructing watertight surfaces from point clouds.

The `IndexedFaceSet` node was designed to store polygon meshes with colors, normals, and/or texture coordinates. In addition to vertex coordinates, colors and normal vectors can be stored bound to vertices. Even though the `IndexedFaceSet` node was not designed to represent point clouds, the standard allows for this node to have vertex coordinates and properties such as colors and/or normals per vertex, but no faces. The standard does not specify how such a node should be rendered in a VRML browser, but since they constitute valid VRML files, they can be used to store point clouds.

The SFL File Format

The SFL file format was introduced with Pointshop3D [ZPKG02] to provide a versatile file format to import and export point clouds with color, normal vectors, and a radius per vertex describing the local sampling density. A SFL file is encoded in binary and features an extensible set of surfel attributes, data compression, upward and downward compatibility, and transparent conversion of surfel attributes, coordinate systems, and color spaces. Pointshop3D is a software system for interactive editing of point-based surfaces, developed at the Computer Graphics Lab at ETH Zurich.

6.1.2 Visualization

A well-established technique to render dense point clouds is point splatting. Each point is regarded as an oriented disk in 3D, with the orientation determined by the surface normal evaluated at each point, and the radius of the disk usually stored as an additional parameter per vertex. As a result, each point is rendered as an ellipse. The color is determined by the color stored with the point, the direction of the normal vector, and the illumination model. The radii are chosen so that the ellipses overlap, resulting in the perception of a continuous surface being rendered.

6.2 Merging Point Clouds

The triangulation-based 3D scanning methods described in previous chapters are able to produce dense point clouds. However, due to visibility constraints these point clouds may have large gaps without samples. In order for a surface point to be reconstructed, it has to be illuminated by a projector, and visible by a camera. In addition, the projected patterns needs to illuminate the surface transversely for the camera to be able to capture a sufficient amount of reflected light. In particular, only points on the front-facing side of the object can be reconstructed (i.e., on the same side as the projector and camera). Some methods to overcome these limitations are discussed in Chapter 7. However, to produce a complete representation, multiple scans taken from various points of view must be integrated to produce a point cloud with sufficient sampling density over the whole visible surface of the object being scanned.

6.2.1 Computing Rigid Body Matching Transformations

The main challenge to merging multiple scans is that each scan is produced with respect to a different coordinate system. As a result, the rigid body transformation needed to register one scan with another must be estimated. In some cases the object is moved with respect to the scanner under computer control. In those cases the transformations needed to register the scans are known within a certain level of accuracy. This is the case when the object is placed on a computer-controlled turntable or linear translation stage. However, when the object is repositioned by hand, the matching transformations are not known and need to be estimated from point correspondences.

We now consider the problem of computing the rigid body transformation $q = Rp + T$ to align two shapes from two sets of N points, $\{p_1, \ldots, p_N\}$ and $\{q_1, \ldots, q_N\}$. That is, we are looking for a rotation matrix R and a translation vector T so that

$$q_1 = Rp_1 + T \quad \ldots \quad q_N = Rp_N + T \; .$$

The two sets of points can be chosen interactively or automatically. In either case, being able to compute the matching transformation in closed form is a fundamental operation.

This registration problem is, in general, not solvable due to measurement errors. A common approach in such a case is to seek a least-squares solution. In this case, we desire a closed-form solution for minimizing the mean squared error

$$\phi(R, T) = \frac{1}{N} \sum_{i=1}^{N} \|Rp_i + T - q_i\|^2 \; , \tag{6.1}$$

over all rotation matrices R and translation vectors T. This yields a quadratic function of 12 components in R and T; however, since R is restricted to be a valid rotation matrix, there exist additional constraints on R. Since the variable T is unconstrained, a closed-form solution for T, as a function of R, can be found by solving the linear system of equations resulting from differentiating the previous expression with respect to T.

$$\frac{1}{2}\frac{\partial \phi}{\partial T} = \frac{1}{N} \sum_{i=1}^{N} (Rp_i + T - q_i) = 0 \Rightarrow T = \overline{q} - R\overline{p}$$

In this expression $\overline{p}$ and $\overline{q}$ are the geometric centroids of the two sets of matching points, given by

$$\overline{p} = \left(\frac{1}{N} \sum_{i=1}^{N} p_i \right) \qquad \overline{q} = \left(\frac{1}{N} \sum_{i=1}^{N} q_i \right) \; .$$

Substituting for T in Equation 6.1, we obtain the following equivalent error function which depends only on R.

$$\psi(R) = \frac{1}{N} \sum_{i=1}^{N} \|R(p_i - \overline{p}) - (q_i - \overline{q})\|^2 \tag{6.2}$$

If we expand this expression we obtain

$$\psi(R) = \frac{1}{N} \sum_{i=1}^{N} \|p_i - \overline{p}\|^2 - \frac{2}{N} \sum_{i=1}^{N} (q_i - \overline{q})^t R(p_i - \overline{p}) + \frac{1}{N} \sum_{i=1}^{N} \|q_i - \overline{q}\|^2 \; ,$$

since $\|Rv\|^2 = \|v\|^2$ for any vector v. As the first and last terms do not depend on R, maximizing this expression is equivalent to maximizing

$$\eta(R) = \frac{1}{N}\sum_{i=1}^{N}(q_i - \overline{q})^t R(p_i - \overline{p}) = \text{trace}(RM) \ ,$$

where M is the 3×3 matrix

$$M = \frac{1}{N}\sum_{i=1}^{N}(p_i - \overline{p})(q_i - \overline{q})^t \ .$$

Recall that, for any pair of matrices A and B of the same dimensions, $\text{trace}(A^tB) = \text{trace}(BA^t)$. We now consider the singular value decomposition (SVD) $M = U\Delta V^t$, where U and V are orthogonal 3×3 matrices, and Δ is a diagonal 3×3 matrix with elements $\delta_1 \geq \delta_2 \geq \delta_3 \geq 0$. Substituting, we find

$$\text{trace}(RM) = \text{trace}(RU\Delta V^t) = \text{trace}((V^tRU)\Delta) = \text{trace}(W\Delta) \ ,$$

where $W = V^tRU$ is orthogonal. If we expand this expression, we obtain

$$\text{trace}(W\Delta) = w_{11}\delta_1 + w_{22}\delta_2 + w_{33}\delta_3 \leq \delta_1 + \delta_2 + \delta_3 \ ,$$

where $W = (w_{ij})$. The last inequality is true because the components of an orthogonal matrix cannot be larger than one. Note that the last inequality is an equality only if $w_{11} = w_{22} = w_{33} = 1$, which is only the case when $W = I$ (the identity matrix). It follows that if V^tU is a rotation matrix, then $R = V^tU$ is the minimizer of our original problem. The matrix V^tU is an orthogonal matrix, but it may not have a negative determinant. In that case, an upper bound for $\text{trace}(W\Delta)$, with W restricted to have a negative determinant, is achieved for $W = J$, where

$$J = \begin{pmatrix} 1 & 0 & 0 \\ 0 & 1 & 0 \\ 0 & 0 & -1 \end{pmatrix} \ .$$

In this case it follows that the solution to our problem is $R = V^tJU$.

6.2.2 The Iterative Closest Point (ICP) Algorithm

The Iterative Closest Point (ICP) is an algorithm employed to match two surface representations, such as points clouds or polygon meshes. This matching algorithm is used to reconstruct 3D surfaces by registering and merging multiple scans. The algorithm is straightforward and can be implemented in real-time. ICP iteratively estimates the transformation (i.e., translation and rotation) between two geometric data sets. The algorithm takes as input two data sets, an initial estimate for the transformation, and an additional criterion for stopping the iterations. The output is an improved estimate of the matching transformation. The algorithm comprises the following steps.

1. Select points from the first shape.
2. Associate points, by nearest neighbor, with those in the second shape.
3. Estimate the closed-form matching transformation using the method derived in the previous section.

4. Transform the points using the estimated parameters.
5. Repeat previous steps until the stopping criterion is met.

The algorithm can be generalized to solve the problem of registering multiple scans. Each scan has an associated rigid body transformation which will register it with respect to the rest of the scans, regarded as a single rigid object. An additional external loop must be added to the previous steps to pick one transformation to be optimized with each pass, while the others are kept constant—either going through each of the scans in sequence, or randomizing the choice.

6.3 Surface Reconstruction from Point Clouds

Watertight surfaces partition space into two disconnected regions so that every line segment joining a point in one region to a point in the other must cross the dividing surface. In this section we discuss methods to reconstruct watertight surfaces from point clouds.

6.3.1 Continuous Surfaces

In mathematics surfaces are represented in parametric or implicit form. A parametric surface $S = \{x(u) : u \in U\}$ is defined by a function $x : U \to \mathbb{R}^3$ on an open subset U of the plane. An implicit surface is defined as a level set $S = \{p \in \mathbb{R}^3 : f(p) = \lambda\}$ of a continuous function $f : V \to \mathbb{R}$, where V is an open subset in 3D. These functions are most often smooth or piecewise smooth. Implicit surfaces are called *watertight* because they partition space into the two disconnected sets of points, one where $f(p) > \lambda$ and a second where $f(p) < \lambda$. Since the function f is continuous, every line segment joining a point in one region to a point in the other must cross the dividing surface. When the boundary surface of a solid object is described by an implicit equation, one of these two sets describes the inside of the object, and the other one the outside. Since the implicit function can be evaluated at any point in 3D space, it is also referred to as a scalar field. On the other hand, parametric surfaces may or may not be watertight. In general, it is difficult to determine whether a parametric surface is watertight or not. In addition, implicit surfaces are preferred in many applications, such as reverse engineering and interactive shape design, because they bound a solid object which can be manufactured; for example, using rapid prototyping technologies or numerically-controlled machine tools, such representations can define objects of arbitrary topology. As a result, we focus our remaining discussion on implicit surfaces.

6.3.2 Discrete Surfaces

A discrete surface is defined by a finite number of parameters. We only consider here polygon meshes, and in particular those polygon meshes representable as `IndexedFaceSet` nodes in VRML files. Polygon meshes are composed of *geometry* and topological *connectivity*. The geometry includes vertex coordinates, normal vectors, and colors (and possibly texture coordinates). The connectivity is represented in various ways. A popular representation used in many isosurface algorithms is the *polygon soup*, where polygon faces are represented as loops of vertex coordinate vectors. If two or more faces share a vertex, the vertex coordinates are repeated as many times as needed. Another popular representation used in isosurface algorithms is the `IndexedFaceSet` (IFS), describing polygon meshes with simply-connected faces. In this representation the geometry is stored as arrays of floating point numbers. In these notes we are primarily concerned with the array `coord` of vertex coordinates, and to a lesser degree with the array `normal` of face normals. The connectivity is described by the total number V of vertices, and F faces, which are

stored in the `coordIndex` array as a sequence of loops of vertex indices, demarcated by values of -1.

6.3.3 Isosurfaces

An isosurface is a polygonal mesh surface representation produced by an isosurface algorithm. An isosurface algorithm constructs a polygonal mesh approximation of a smooth implicit surface $S = \{x : f(x) = 0\}$ within a bounded three-dimensional volume, from samples of a defining function $f(x)$ evaluated on the vertices of a volumetric grid. Marching Cubes [LC87] and related algorithms operate on function values provided at the vertices of hexahedral grids. Another family of isosurface algorithms operate on functions evaluated at the vertices of tetrahedral grids [DK91]. Usually, no additional information about the function is provided, and various interpolation schemes are used to evaluate the function within grid cells, if necessary. The most natural interpolation scheme for tetrahedral meshes is linear interpolation, which we also adopt here.

6.3.4 Isosurface Construction Algorithms

An isosurface algorithm producing a polygon soup output must solve three key problems: (1) determining the quantity and location of isosurface vertices within each cell, (2) determining how these vertices are connected forming isosurface faces, and (3) determining globally consistent face orientations. For isosurface algorithms producing IFS output, there is a fourth problem to solve: identifying isosurface vertices lying on vertices and edges of the volumetric grid. For many visualization applications, the polygon soup representation is sufficient and acceptable, despite the storage overhead. Isosurface vertices lying on vertices and edges of the volumetric grid are independently generated multiple times. The main advantage of this approach is that it is highly parallelizable. But, since most of these boundary vertices are represented at least twice, it is not a compact representation.

Researchers have proposed various solutions and design decisions (e.g., cell types, adaptive grids, topological complexity, interpolant order) to address these four problems. The well-known Marching Cubes (MC) algorithm uses a fixed hexahedral grid (i.e., cube cells) with linear interpolation to find zero-crossings along the edges of the grid. These are the vertices of the isosurface mesh. Second, polygonal faces are added connecting these vertices using a table. The crucial observation made with MC is that the possible connectivity of triangles in a cell can be computed independently of the function samples and stored in a table. Out-of-core extensions, where sequential layers of the volume are processed one at a time, are straightforward.

Similar tetrahedral-based algorithms [DK91, GH95, TPG99], dubbed Marching Tetrahedra (MT), have also been developed (again using linear interpolation). Although the cell is simpler, MT requires maintaining a tetrahedral sampling grid. Out-of-core extensions require presorted traversal schemes, such as in [CS97]. For an unsorted tetrahedral grid, hash tables are used to save and retrieve vertices lying on edges of the volumetric grid. As an example of an isosurface algorithm, we discuss MT in more detail.

Marching Tetrahedra

MT operates on the following input data: (1) a tetrahedral grid and (2) one piecewise linear function $f(x)$, defined by its values at the grid vertices. Within the tetrahedron with vertices

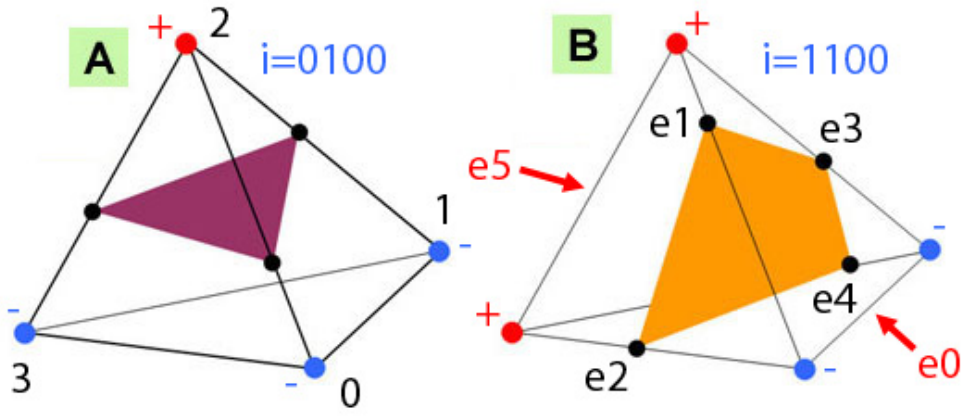

Figure 6.1: In isosurface algorithms, the sign of the function at the grid vertices determines the topology and connectivity of the output polygonal mesh within each tetrahedron. Mesh vertices are located on grid edges where the function changes sign.

$x_0, x_1, x_2, x_3 \in \mathbb{R}^3$, the function is linear and can be described in terms of the barycentric coordinates $b = (b_0, b_1, b_2, b_3)^t$ of an arbitrary internal point $x = b_0\, x_0 + b_1\, x_1 + b_2\, x_2 + b_3\, x_3$ with respect to the four vertices: $f(x) = b_0\, f(x_0) + b_1\, f(x_1) + b_2\, f(x_2) + b_3\, f(x_3)$, where $b_0, b_1, b_2, b_3 \geq 0$ and $b_0 + b_1 + b_2 + b_3 = 1$. As illustrated in Figure 6.1, the sign of the function at the four grid vertices determines the connectivity (e.g., triangle, quadrilateral, or empty) of the output polygonal mesh within each tetrahedron. There are actually $16 = 2^4$ cases, which modulo symmetries and sign changes reduce to only three. Each grid edge, whose end vertex values change sign, corresponds to an isosurface mesh vertex. The exact location of the vertex along the edge is determined by linear interpolation from the actual function values, but note that the 16 cases can be precomputed and stored in a table indexed by a 4-bit integer $i = (i_3 i_2 i_1 i_0)$, where $i_j = 1$ if $f(x_j) > 0$ and $i_j = 0$, if $f(x_j) < 0$. The full table is shown in Table 6.1. The cases $f(x_j) = 0$ are singular and require special treatment. For example, the index is $i = (0100) = 4$ for Figure 6.1(a), and $i = (1100) = 12$ for Figure 6.1(b). Orientation for the isosurface faces, consistent with the orientation of the containing tetrahedron, can be obtained from connectivity alone (and are encoded in the look-up table as shown in Table 6.1). For IFS output it is also necessary to stitch vertices as described above.

Algorithms to polygonize implicit surfaces [Blo88], where the implicit functions are provided in analytic form, are closely related to isosurface algorithms. For example, Bloomenthal and Ferguson [BF95] extract non-manifold isosurfaces produced from trimming implicits and parameterics using a tetrahedral isosurface algorithm. [WvO96] polygonize boolean combinations of skeletal implicits (Boolean Compound Soft Objects), applying an iterative solver and face subdivision for placing vertices along feature edges and points. Suffern and Balsys [SB03] present an algorithm to polygonize surfaces defined by two implicit functions provided in analytic form; this same algorithm can compute bi-iso-lines of pairs of implicits for rendering.

Isosurface Algorithms on Hexahedral Grids

An isosurface algorithm constructs a polygon mesh approximation of a level set of a scalar function defined in a finite 3D volume. The function $f(p)$ is usually specified by its values $f_\alpha = f(p_\alpha)$

i	$(i_3 i_2 i_1 i_0)$	face
0	0000	[-1]
1	0001	[2,1,0,-1]
2	0010	[0,3,4,-1]
3	0011	[1,3,4,2,-1]
4	0100	[1,5,3,-1]
5	0101	[0,2,5,3,-1]
6	0110	[0,3,5,4,-1]
7	0111	[1,5,2,-1]
8	1000	[2,5,1,-1]
9	1001	[4,5,3,0,-1]
10	1010	[3,5,2,0,-1]
11	1011	[3,5,1,-1]
12	1100	[2,4,3,1,-1]
13	1101	[4,3,0,-1]
14	1110	[0,1,2,-1]
15	1111	[-1]

e	edge
0	(0,1)
1	(0,2)
2	(0,3)
3	(1,2)
4	(1,3)
5	(2,3)

Table 6.1: Look-up tables for tetrahedral mesh isosurface evaluation. Note that consistent face orientation is encoded within the table. Indices stored in the first table reference tetrahedron edges, as indicated by the second table of vertex pairs (and further illustrated in Figure 6.1). In this case, only edge indices $\{1, 2, 3, 4\}$ have associated isosurface vertex coordinates, which are shared with neighboring cells.

on a regular grid of three dimensional points

$$G = \{p_\alpha : \alpha = (\alpha_0, \alpha_1, \alpha_2) \in [\![n_0]\!] \times [\![n_1]\!] \times [\![n_2]\!]\} \ ,$$

where $[\![n_j]\!] = \{0, \ldots, n_j - 1\}$, and by a method to interpolate in between these values. The surface is usually represented as a polygon mesh, and is specified by its *isovalue* f_0. Furthermore, the interpolation scheme is assumed to be linear along the edges of the grid, so that the isosurface cuts each edge in no more than one point. If p_α and p_β are grid points connected by an edge, and $f_\alpha > f_0 > f_\beta$, the location of the point $p_{\alpha\beta}$ where the isosurface intersects the edge is

$$p_{\alpha\beta} = \frac{f_\alpha - f_0}{f_\alpha - f_\beta} \, p_\beta + \frac{f_\beta - f_0}{f_\beta - f_\alpha} \, p_\alpha \ . \tag{6.3}$$

Marching Cubes

One of the most popular isosurface extraction algorithms is *Marching Cubes* [LC87]. In this algorithm the points defined by the intersection of the isosurface with the edges of the grid are the vertices of the polygon mesh. These vertices are connected forming polygon faces according to the following procedure. Each set of eight neighboring grid points define a small cube called a *cell*

$$C_\alpha = \{p_{\alpha+\beta} : \beta \in \{0, 1\}^3\}.$$

Since the function value associated with each of the eight corners of a cell may be either above or below the isovalue (isovalues equal to grid function values are called singular and should be avoided), there are $2^8 = 256$ possible configurations. A polygonization of the vertices within each cell, for each one of these configurations, is stored in a static look-up table. When symmetries are taken into account, the size of the table can be reduced significantly.

6.3.5 Algorithms to Fit Implicit Surfaces to Point Clouds

Let U be a relatively open and simply-connected subset of $\mathbb{R}^3$, and $f : U \to \mathbb{R}$ a smooth function. The gradient ∇f is a vector field defined on U. Given an *oriented point cloud*, i.e., a finite set $\mathcal{D}$ of point-vector pairs (p, n), where p is an interior point of U, and n is a unit length 3D vector, the problem is to find a smooth function f so that $f(p) \approx 0$ and $\nabla(p) \approx n$ for every oriented point (p, n) in the data set $\mathcal{D}$. We call the zero iso-level set of such a function $\{p : f(p) = 0\}$ a *surface fit*, or *surface reconstruction*, for the data set $\mathcal{D}$.

We are particularly interested in fitting isosurfaces to oriented point points. For the sake of simplicity, we assume that the domain is the unit cube $U = [0, 1]^3$, the typical domain of an isosurface defined on an hexahedral mesh, and the isolevel is zero, i.e., the isosurface to be fitted to the data points is $\{p : f(p) = 0\}$, but of course, the argument applies in more general cases.

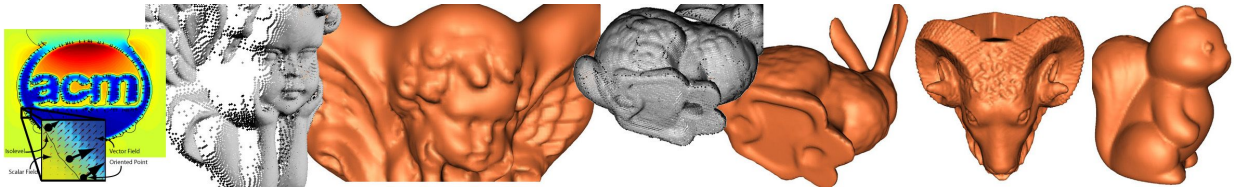

Figure 6.2: Early results of Vector Field Isosurface reconstruction from oriented point clouds introduced in [ST05].

Figure 6.2 shows results of surface reconstruction from an oriented point cloud using the simple variational formulation presented in [ST05], where oriented data points are regarded as samples of the gradient vector field of an implicit function, which is estimated by minimizing this energy function

$$E_1(f) = \sum_{i=1}^{m} f(p_i)^2 + \lambda_1 \sum_{i=1}^{m} \|\nabla f(p_i) - n_i\|^2 + \lambda_2 \int_V \|Hf(x)\|^2 \, dx \,, \tag{6.4}$$

where $f(x)$ is the implicit function being estimated, $\nabla f(x)$ is the gradient of f, $Hf(x)$ is the Hessian of $f(x)$, $(p_1, n_1), \ldots, (p_m, n_m)$ are point-normal data pairs, V is a bounding volume, and λ_1 and λ_2 are regularization parameters. Minimizing this energy requires the solution of a simple large and sparse least squares problem. The result is usually unique modulo an additive constant. Given that, for rendering or post-processing, isosurfaces are extracted from scalar functions defined over regular grids (e.g., via Marching Cubes), it is worth exploring representations of implicit functions defined as a regular scalar fields. Finite difference discretization is used in [ST05], with the volume integral resulting in a sum of gradient differences over the edges of the regular grid, yet Equation 6.4 can be discretized in many other ways.

Chapter 7

Conclusion

As low-cost mobile projectors enter the market, we expect students and hobbyists to begin incorporating them into their own 3D scanning systems. Such projector-camera systems have already received a great deal of attention in recent academic publications. Whether for novel human-computer interaction or ad-hoc tiled displays, consumer digital projection is set to revolutionize the way we interact with both physical and virtual assets.

This course was designed to lower the barrier of entry to novices interested in trying 3D scanning in their own projects. Through the course notes, on-line materials, and open source software, we have endeavored to eliminate the most difficult hurdles facing beginners. We encourage attendees to email the authors with questions or links to their own 3D scanning projects that draw on the course material. Revised course notes, updated software, recent publications, and similar do-it-yourself projects are maintained on the course website at `http://mesh.brown.edu/byo3d`. We encourage you to take a look and see what your fellow attendees have built for themselves!

Bibliography

[Na13] NATIONAL INSTRUMENTS CORP.: *Choosing the Right Camera Bus*, http://www.ni.com/white-paper/5386/en/. Tech. rep., 2013. 20

[AHH10] ATCHESON B., HEIDE F., HEIDRICH W.: CALTag: High precision fiducial markers for camera calibration. In 15th *International Workshop on Vision, Modeling and Visualization* (Siegen, Germany, Nov. 2010). 22, 29

[BF95] BLOOMENTHAL J., FERGUSON K.: Polygonization of non-manifold implicit surfaces. In *SIGGRAPH '95: ACM SIGGRAPH 1995 papers* (1995), pp. 309–316. 53

[Bla04] BLAIS F.: Review of 20 years of range sensor development. *Journal of Electronic Imaging 13*, 1 (2004), 231–240. 3

[Blo88] BLOOMENTHAL J.: Polygonization of Implicit Surfaces. *Computer Aided Geometric Design 5*, 4 (1988), 341–355. 53

[Bou] BOUGUET J.-Y.: Camera calibration toolbox for matlab. http://www.vision.caltech.edu/bouguetj/calib_doc/. 25

[CG00] CIPOLLA R., GIBLIN P.: *Visual Motion of Curves and Surfaces*. Cambridge University Press, 2000. 3

[CMU] CMU IEEE 1394 digital camera driver, version 6.4.5. http://www.cs.cmu.edu/ iwan/1394/. 20

[Cre] CREAFORM: Handyscan 3D. http://www.creaform3d.com/en/handyscan3d/products/exascan.aspx. 4

[CS97] CHIANG Y., SILVA C. T.: I/O Optimal Isosurface Extraction. In *IEEE Visualization 1997, Conference Proceedings* (1997), pp. 293–300. 52

[CTMS03] CARRANZA J., THEOBALT C., MAGNOR M. A., SEIDEL H.-P.: Free-viewpoint video of human actors. *ACM Trans. Graph. 22*, 3 (2003), 569–577. 3

[dAST*08] DE AGUIAR E., STOLL C., THEOBALT C., AHMED N., SEIDEL H.-P., THRUN S.: Performance capture from sparse multi-view video. In *SIGGRAPH '08: ACM SIGGRAPH 2008 papers* (2008), pp. 1–10. 3

[Deb97] DEBEVEC P. E.: Facade: modeling and rendering architecture from photographs and the campanile model. In *SIGGRAPH '97: ACM SIGGRAPH 97 Visual Proceedings* (1997), p. 254. 3

[DK91] DOI A., KOIDE A.: An Efficient Method of Triangulating Equivalued Surfaces by Using Tetrahedral Cells. *IEICE Transactions on Communications and Electronics Information Systems E74*, 1 (Jan. 1991), 214–224. 52

[Far97] FARID H.: *Range Estimation by Optical Differentiation*. PhD thesis, University of Pennsylvania, 1997. 3

[FWM98] FERRYMAN J. M., WORRALL A. D., MAYBANK S. J.: Learning enhanced 3d models for vehicle tracking. In *BMVC* (1998), pp. 873–882. 3

[GH95] GUÉZIEC A., HUMMEL R.: Exploiting Triangulated Surface Extraction Using Tetrahedral Decomposition. *IEEE Transactions on Visualization and Computer Graphics 1*, 4 (1995). 52

[GSP06] GREENGARD A., SCHECHNER Y. Y., PIESTUN R.: Depth from diffracted rotation. *Opt. Lett. 31*, 2 (2006), 181–183. 3

[HARN06] HSU S., ACHARYA S., RAFII A., NEW R.: Performance of a time-of-flight range camera for intelligent vehicle safety applications. *Advanced Microsystems for Automotive Applications* (2006). 5

[Hec01] HECHT E.: *Optics (4th Edition)*. Addison Wesley, 2001. 3

[HVB*07] HERNÁNDEZ C., VOGIATZIS G., BROSTOW G. J., STENGER B., CIPOLLA R.: Non-rigid photometric stereo with colored lights. In *Proc. of the 11th IEEE Intl. Conf. on Comp. Vision (ICCV)* (2007). 5

[HZ04] HARTLEY R. I., ZISSERMAN A.: *Multiple View Geometry in Computer Vision*, second ed. Cambridge University Press, 2004. 2, 21

[ISM84] INOKUCHI S., SATO K., MATSUDA F.: Range imaging system for 3-d object recognition. In *Proceedings of the International Conference on Pattern Recognition* (1984), pp. 806–808. 41

[IY01] IDDAN G. J., YAHAV G.: Three-dimensional imaging in the studio and elsewhere. *Three-Dimensional Image Capture and Applications IV 4298*, 1 (2001), 48–55. 5

[KM00] KAKADIARIS I., METAXAS D.: Model-based estimation of 3d human motion. *IEEE Transactions on Pattern Analysis and Machine Intelligence 22*, 12 (2000), 1453–1459. 3

[Las] LASER DESIGN INC.: Surveyor DT-2000 desktop 3D laser scanner. http://www.laserdesign.com/quick-attachments/hardware/low-res/dt-series.pdf. 4

[Lau94] LAURENTINI A.: The Visual Hull Concept for Silhouette-Based Image Understanding. *IEEE TPAMI 16*, 2 (1994), 150–162. 3

[LC87] LORENSEN W. L., CLINE H. E.: Marching Cubes: A High Resolution 3D Surface Construction Algorithm. In *Siggraph'87, Conference Proceedings* (1987), ACM Press, pp. 163–169. 52, 54

[LFDF07] LEVIN A., FERGUS R., DURAND F., FREEMAN W. T.: Image and depth from a conventional camera with a coded aperture. *ACM Trans. Graph. 26*, 3 (2007), 70. 3

[LHKP13] LI B., HENG L., KOSER K., POLLEFEYS M.: A multiple-camera system calibration toolbox using a feature descriptor-based calibration pattern. In *Intelligent Robots and Systems (IROS), 2013 IEEE/RSJ International Conference on* (2013), IEEE, pp. 1301–1307. 22

[LN04] LAND M. F., NILSSON D.-E.: *Animal Eyes*. Oxford University Press, 2004. 2

[Mat] MATHWORKS, INC: Image acquisition toolbox. http://www.mathworks.com/products/imaq/. 20

[MBR*00] MATUSIK W., BUEHLER C., RASKAR R., GORTLER S. J., MCMILLAN L.: Image-based visual hulls. In *SIGGRAPH '00: ACM SIGGRAPH 2000 papers* (2000), pp. 369–374. 3

[mes] Meshlab 3D viewer. http://meshlab.sourceforge.net/. 46

[MPL04] MARC R. Y., POLLEFEYS M., LI S.: Improved real-time stereo on commodity graphics hardware. In *In IEEE Workshop on Real-time 3D Sensors and Their Use* (2004). 2

[MSKS05] MA Y., SOATTO S., KOSECKA J., SASTRY S. S.: *An Invitation to 3-D Vision*. Springer, 2005. 21

[MT] MORENO D., TAUBIN G.: Projector-Camera Calibration and Scanning Software. http://mesh.brown.edu/scanning/software.html. 25, 43, 44

[MT12] MORENO D., TAUBIN G.: Simple, accurate, and robust projector-camera calibration. In *3D Imaging, Modeling, Processing, Visualization and Transmission (3DIMPVT), 2012 Second International Conference on* (2012), IEEE, pp. 464–471. 19, 24

[Nex] NEXTENGINE: 3D Scanner HD. https://www.nextengine.com/indexSecure.htm. 4

[NN94] NAYAR S. K., NAKAGAWA Y.: Shape from focus. *IEEE Trans. Pattern Anal. Mach. Intell. 16*, 8 (1994), 824–831. 3

[Ope] Open source computer vision library. http://opencv.org. 20

[OSS*00] ORMONEIT D., SIDENBLADH H., SIDENBLADH H., BLACK M. J., HASTIE T., FLEET D. J.: Learning and tracking human motion using functional analysis. In *IEEE Workshop on Human Modeling, Analysis and Synthesis* (2000), pp. 2–9. 3

[PA82] POSDAMER J., ALTSCHULER M.: Surface measurement by space encoded projected beam systems. *Computer Graphics and Image Processing 18* (1982), 1–17. 41

[Poi] POINT GREY RESEARCH, INC.: Grasshopper IEEE-1394b digital camera. http://www.ptgrey.com/products/grasshopper/index.asp. 20

[Pol] POLHEMUS: FastSCAN. http://www.polhemus.com/?page=Scanning_Fastscan. 4

[RWLB01] RASKAR R., WELCH G., LOW K.-L., BANDYOPADHYAY D.: Shader lamps: Animating real objects with image-based illumination. In *Proceedings of the 12th Eurographics Workshop on Rendering Techniques* (2001), Springer-Verlag, pp. 89–102. 3

[SB03] SUFFERN K. G., BALSYS R. J.: Rendering the intersections of implicit surfaces. *IEEE Comput. Graph. Appl. 23*, 5 (2003), 70–77. 53

[SCD*06] SEITZ S., CURLESS B., DIEBEL J., SCHARSTEIN D., SZELISKI R.: A comparison and evaluation of multi-view stereo reconstruction algorithms. In *CVPR 2006* (2006). 2

[SFPL10] SALVI J., FERNANDEZ S., PRIBANIC T., LLADO X.: A state of the art in structured light patterns for surface profilometry. *Pattern recognition 43*, 8 (2010), 2666–2680. 39

[SH03] STARCK J., HILTON A.: Model-based multiple view reconstruction of people. In *Proceedings of the Ninth IEEE International Conference on Computer Vision* (2003), p. 915. 3

[Sim] Computer vision platform using python. http://http://simplecv.org/. 20

[SMP05] SVOBODA T., MARTINEC D., PAJDLA T.: A convenient multi-camera self-calibration for virtual environments. *PRESENCE: Teleoperators and Virtual Environments 14*, 4 (August 2005), 407–422. 22

[SPB04] SALVI J., PAGÈS J., BATLLE J.: Pattern codification strategies in structured light systems. In *Pattern Recognition* (April 2004), vol. 37, pp. 827–849. 4

[ST05] SIBLEY P. G., TAUBIN G.: Vectorfield Isosurface-based Reconstruction from Oriented points. In *SIGGRAPH'05 Sketch* (2005). 55

[Sul95] SULLIVAN G.: Model-based vision for traffic scenes using the ground-plane constraint. 93–115. 3

[TPG99] TREECE G. M., PRAGER R. W., GEE A. H.: Regularised Marching Tetrahedra: Improved Iso-Surface Extraction. *Computers and Graphics 23*, 4 (1999), 583–598. 52

[VF92] VAILLANT R., FAUGERAS O. D.: Using extremal boundaries for 3-d object modeling. *IEEE Trans. Pattern Anal. Mach. Intell. 14*, 2 (1992), 157–173. 2

[Wik] WIKIPEDIA: Gray code. http://en.wikipedia.org/wiki/Gray_code. 42

[WN98] WATANABE M., NAYAR S. K.: Rational filters for passive depth from defocus. *Int. J. Comput. Vision 27*, 3 (1998), 203–225. 3

[Woo89] WOODHAM R. J.: Photometric method for determining surface orientation from multiple images. 513–531. 5

[WvO96] WYVILL B., VAN OVERVELD K.: Polygonization of Implicit Surfaces with Constructive Solid Geometry. *Journal of Shape Modelling 2*, 4 (1996), 257–274. 53

[XA07] XU Y., ALIAGA D. G.: Robust pixel classification for 3d modeling with structured light. In *Proceedings of Graphics Interface 2007* (2007), ACM, pp. 233–240. 43

[Zha00] ZHANG Z.: A flexible new technique for camera calibration. *IEEE Trans. Pattern Anal. Mach. Intell. 22*, 11 (2000), 1330–1334. 19, 21

[ZPKG02] ZWICKER M., PAULY M., KNOLL O., GROSS M.: Pointshop 3d: an interactive system for point-based surface editing. *ACM Trans. Graph. 21*, 3 (2002), 322–329. 48